UNIVERSITY OF CALIFORNIA

Santa Barbara

Design, Synthesis and Theoretical Investigation of Small Molecules for Utility in Organic Semiconducting Devices

A dissertation submitted in partial satisfaction of the

requirements for the degree Doctor of Philosophy

in Chemistry

by

Thomas S. van der Poll

Committee in charge:

Professor Guillermo C. Bazan, Chair

Professor Thuc-Quyen Nguyen

Professor Craig J. Hawker

Professor Javier Read de Alaniz

June 2014

The dissertation of Thomas S. van der Poll is approved.

_____
Thuc-Quyen Nguyen

_____
Craig J. Hawker

_____
Javier Read de Alaniz

_____
Guillermo C. Bazan, Committee Chair

May 2014

Design, Synthesis and Theoretical Investigation of Small Molecules for Utility in Organic Semiconducting Devices

by

Thomas S. van der Poll

ACKNOWLEDGEMENTS

I'd like to Professor Guillermo C. Bazan for the opportunity to do cutting edge research at the frontier of energy science. Without him none of my intellectual contributions would be possible, nor would the numerous invaluable experiences and opportunities I have benefited from in my tenure as a graduate student. I would like to give special thanks to Professor Gregory Welch for being a good friend and a caliber of scientist I aspire to be. Many of my colleagues have become lifelong friends in no small part due to their untiring support and encouragement, especially Zac Henson, Adam Pollak, Michelle Kem, and Ron Bakus.

I'd like to thank my brothers Herbert, Maarten and Derek who I hold the highest levels of respect and love for. Their support and friendship has carried me through all stages of my life and I am eternally grateful. I'd like to thank my amazing fiancé, Dr. Hannah Zane, for being there every single day and making my life so much better. Finally, my mother and father, Henny and Jan, are my biggest supporters and best friends. I could not have come this far without you.

VITA OF THOMAS SCOTT VAN DER POLL

May 2014

EDUCATION

Bachelor of Science, University of Massachusetts, Amherst, May 2009 (summa cum laude)
Doctor of Philosophy in Chemistry, University of California, Santa Barbara, May 2014 (expected)

PROFESSIONAL EMPLOYMENT

2009-2014: Teaching Assistant, Department of Chemistry, University of California, Santa Barbara

Summer 2013: Summer Internship, Los Alamos National Laboratory

PUBLICATIONS

"Pyridalthiadiazole-Based Narrow Band Gap Chromophores," Z. B. Henson, G. C. Welch, T. van der Poll, and G. C. Bazan, *J. Am. Chem. Soc.* **2012**, *134*, 3766-3779.

"Non-Basic High-Performance Molecules for Solution-Processed Organic Solar Cells," T. S. van der Poll, J. A. Love, T.-Q. Nguyen, and G. C. Bazan, *Adv. Mater.* **2012**, *24*, 3646-3649.

"Film Morphology of High Efficiency Solution-Processed Small-Molecule Solar Cells," J. A. Love, C. M. Proctor, J. Liu, C. J. Takacs, A. Sharenko, T. S. van der Poll, A. J. Heeger, G. C. Bazan, T.-Q. Nguyen, *Adv. Funct. Mater.* **2013**, *23*, 5019-5026

"A High-Performance Solution-Processed Small Molecule:Perylene Diimide Bulk Heterojunction Solar Cell," A. Sharenko, C. M. Proctor, T. S. van der Poll, Z. B. Henson, T.-Q. Nguyen, G. C. Bazan, *Adv. Mater.* **2013**, *25*, 4403-4406.

"Solvent Additive Effects on Small Molecule Crystallization in Bulk Heterojunction Solar Cells Probed During Spin-Casting," L. A. Perez, K. W. Chou, J. A. Love, T. S. van der Poll, D.-M. Smilgies, T.-Q. Nguyen, E. J. Kramer, A. Amassian, G. C. Bazan, *Adv. Mater.* **2013**, *25*, 6380-6384.

"Formation of Interfacial Traps Upon Surface Protonation in Small Molecule Solution Processed Bulk Heterojunctions Probed by Photoelectron Spectroscopy" E. L. Ratcliff, R. C. Bakus II, G. C. Welch, T. S. van der Poll, A Garcia, S. R. Cowan,

B. A. Macleod, D. S. Ginley, G. C. Bazan, D. C. Olson, *J. Mater. Chem. C.* **2013**, *1*, 6223-6234

"Ultrafast Long-Range Charge Separation in Organic Semiconductor Photovoltaic Diodes," S. Gélinas, A. Rao, A. Kumar, S. L. Smith, A. W. Chin, J. Clark, T. S. van der Poll, G. C. Bazan, R. H. Friend, *Science*. **2013**, *343*, 512-516.

"Silaindacenodithiophene-Based Molecular Donor: Morphological Features and Us in the Fabrication of Compositionally Tolerant, High-Efficiency Bulk Heterojunction Solar Cells" J. A. Love, I. Nagao, Y. Huang, M. Kuik, V. Gupta, C. J. Takacs, J. E. Coughlin, L. Qi, T. S. van der Poll, E. J. Kramer, A. J. Heeger, T.-Q. Nguyen, G. C. Bazan, *J. Am. Chem. Soc.* **2014**, *136*, 3597-3606.

PATENTS

"Inert Solution-Processable Molecular Chromophores for Organic Electronic Devices", G. C. Bazan, T. S. van der Poll, T.-Q. Nguyen, J. A. Love, *US Patent & Trademark Office.* **2013**, Publication No: US 20130247989 A1.

PRESENTATIONS

"Design and Synthesis of Organic Semiconductors for Solution-Processed Bulk Heterojunction Solar Cells," Center for Polymers and Organic Solids, University of California, Santa Barbara, January 17, 2012. (Invited)

"Simple Substitution Influence on Molecular Packing & Direct Arylation for Generating High-Performance Materials for Organic Photovoltaics," Internal Semi-Annual Review of Center for Energy Efficient Materials, an Energy Frontier Research Center funded by the Office of Basic Energy Sciences of the US Department of Energy. July 24, 2012.

"New Organic Semiconductors for World Record Solution-Processed Solar Cells," External Review of Center for Energy Efficient Materials, an Energy Frontier Research Center funded by the Office of Basic Energy Sciences of the US Department of Energy. March 5, 2012. (Poster)

"Design and Synthesis of Organic Semiconductors for Solution-Processed Bulk Heterojunction Solar Cells," Spring 2012 ACS Meeting, San Diego, California, March 25-29, 2012. (Oral)

"Non-Basic High-Performance Molecules for Solution Processed Solar Cells," Organic Solar Cells, Conference, Santa Fe, New Mexico, May 6-8, 2013. (Poster)

"Non-Basic Small Molecule Semiconductor with World-Record Organic Photovoltaic Efficiency," Energy Frontier Research Meeting PI Meeting, Washington D. C., July 18-19, 2013. (Poster)

AWARDS

Department of Chemistry fellowship, University of California, Santa Barbara, 2009

FIELDS OF STUDY

Major Field: Materials Chemistry; Organic Semiconductors

Studies in Molecular Design and Synthesis with Professor Guillermo C. Bazan

Studies in Computational Chemistry with Professor Sergei Tretiak

ABSTRACT

Design, Synthesis and Theoretical Investigation of Small Molecules for Utility in Organic Semiconducting Devices

by

Thomas S. van der Poll

Solution-processed small molecule bulk-heterojunction solar cells represent a specific subset of organic photovoltaics (OPV). OPV devices rely on materials with appropriately aligned frontier molecular orbitals, bandgaps commensurate with the solar spectrum, and ultimately must self-assemble into a morphology conducive to high device performance. Optical electronic and physical properties in organic materials are highly sensitive to their chemical structure and the conformations of those structures in space. Materials can be engineered to exhibit specific traits; a process referred to as "molecular design." While the molecular design toolbox is ever-expanding, each of these properties requires unique considerations, and indeed vary greatly in the degree of control the synthetic chemist has in producing predictable properties. In order to elucidate the relationship between structure and properties, a class of small molecules was developed adhering to what can be described as a D'ADAD' architecture, where D, D' and A refer to an electron rich

core, electron rich end-caps and electron deficient heterocyclic fragments, respectively. These fragments, as well as solubilizing side groups were systematically modified, yielding useful design rules for organic donor materials as well as record breaking small-molecule OPV devices. The top performing material in the group exhibited diminutive performance on the ubiquitous solution deposited substrate PEDOT:PSS due to interfacial chemistry. This led to the development of a new material, p-DTS($FBTTh_2$)$_2$, which was not susceptible to the interfacial chemistry with PEDOT:PSS, and broke the previous performance record for solution-processed small molecule OPV devices. Four isostructural molecules, including p-DTS($FBTTh_2$)$_2$ were investigated with single crystal x-ray diffraction. While all four molecules appear topologically equivalent, two types of crystal structure were observed with distinct crystal systems and each with a characteristic molecular geometry. A multi-scale theoretical investigation of simulated isolated molecules and experimentally determined crystal structures offers a clear explanation for the observed lattices, where useful experimental data is unavailable.

TABLE OF CONTENTS

LIST OF FIGURES

I. Introduction and Overview

Academic research has sustained steady improvement in organic photovoltaic technology for nearly two decades, and in the last few years, double-digit efficiencies have been achieved. Solution-processed polymer/fullerene bulk-heterojunction solar cells have dominated the frontier of high-performance devices through an ever-deepening understanding of material design strategies, device architectures and fabrication methods. However, more recently small molecule donor materials have offered some key advantages whereby sharp improvements in device performance have rendered them a competitive alternative to polymers. The work presented focuses on advancing organic photovoltaic technology using both experiment and theory. In this chapter, context is provided first by briefly discussing the development of modern semiconducting organic materials, and then some of the techniques and strategies for manipulating material properties.

A. Background

Organic photovoltaics comprise numerous types of materials, device architectures and preparation styles.[1-6] Solution-processed (SP) bulk-heterojunction (BHJ) solar cells are one subset, wherein two components, a "donor" material and an "acceptor" material are dissolved together and cast from solution to produce the active layer, where the photovoltaic effect occurs.[7] The donor material is so named because it donates an electron to the acceptor. The two components are necessary to provide a sufficient driving force for charge separation, given the low dielectric

constants of organic materials. The operating mechanism can be broken into four steps: 1) photoexcitation, or exciton formation 2) exciton diffusion, 3) exciton dissociation and 4) charge transport and collection. These processes take places in the highest occupied molecular orbital (HOMO) and the lowest unoccupied molecular orbital (LUMO) of the active layer materials, as illustrated in Figure 1-1.

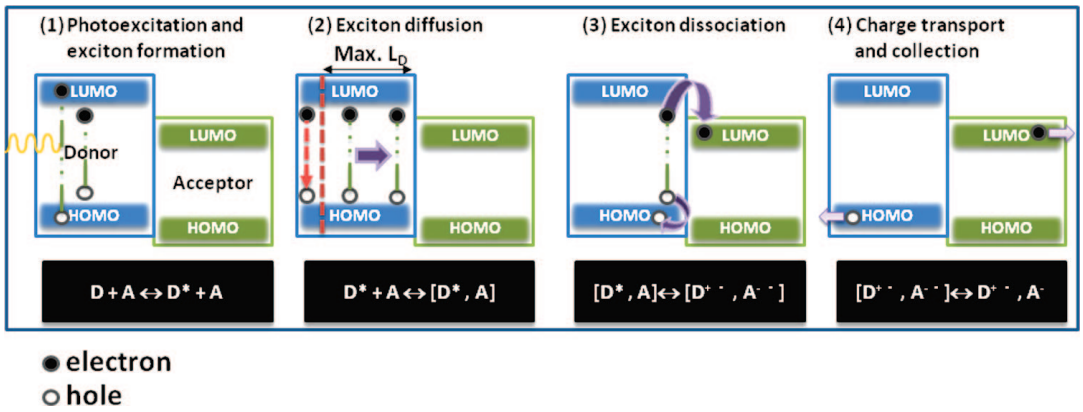

Figure 1-1. Graphical representation of photovoltaic mechanism in BHJ OPV devices.

Typically step 1, and in turn step 2, occur in the donor phase where the majority of photons are absorbed. While the acceptor can absorb photons, the most efficacious examples of BHJ solar cells employ fullerene derivatives in that role, whose unique and useful n-type characteristics outweigh their less useful band gaps and oscillator strengths.[8] On the other hand, π-conjugated polymers exhibit long-range electronic delocalization, allowing for absorption of low energy radiation and good charge carrier mobilities.[9-14] The key to molecular design in this case is that the careful selection of repeat units to be incorporated into polymer architectures systematically

modulates the properties of the resulting material. An additional advantage associated with polymers is the fact that by virtue of their high molecular weights, they typically form viscous solutions, which allows for greater control and reproducibility in the thickness and quality of solution processed films; one of the facts ascribed to the comparatively low performance of small, molecular species in the past. It follows that polymers dominated academic efforts in OPV; however, in the last five years, small molecules have garnered a great deal of attention, as advancements in molecular design have unveiled avenues to circumvent their intrinsic limitations.[15,16] The next section provides a brief overview of how actual lab-scale photovoltaic devices are produced and how they operate, followed by some of the fundamental design principles for molecular organic photovoltaic donor materials.

B. Lab-scale OPV Devices

To understand what material properties are important in a donor material, it is helpful to consider the design and construction of a typical lab-scale BHJ OPV device. As illustrated in Figure 1-2, the preparation starts with a clean transparent electrode, upon which an interlayer may or may not deposited in order to selectively transport charge carriers. Next, a blend solution of donor and acceptor material is spun-cast onto the aforementioned substrate, followed by the optional deposition of another interlayer, and finally a counter-electrode.

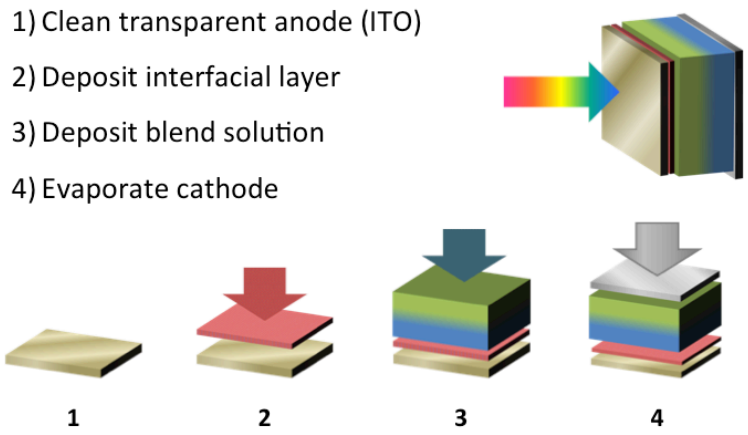

Figure 1-2. Device preparation for standard OPV architecture.

The size, distribution, continuity and molecular ordering in donor and acceptor domains play a crucial role in device performance.[4,17-21] Photoexcitation occurs in the bulk, after which the exciton must diffuse to a donor-acceptor interface. Since the exciton has a limited diffusion length, excitons formed too far from a donor-acceptor interface ultimately cannot be harvested. Also, excitons formed in domains with no path to an electrode are also un-harvestable. Following that logic, the typical idealized BHJ possesses continuous interpenetrating domains such that every exciton is formed within diffusing distance of a donor-acceptor interface. There are currently no practical methods to reproduce an idealized BHJ or to manipulate exciton diffusion length, but there are many strategies to optimize other important material properties that improve photovoltaic performance.

Power conversion efficiency (PCE) is assessed by illuminating devices with simulated solar radiation and measuring current density as a function of an applied

potential. The curve generated from those data yields metrics by which an overall PCE is calculated, as in the example curve shown in Figure 1-3.

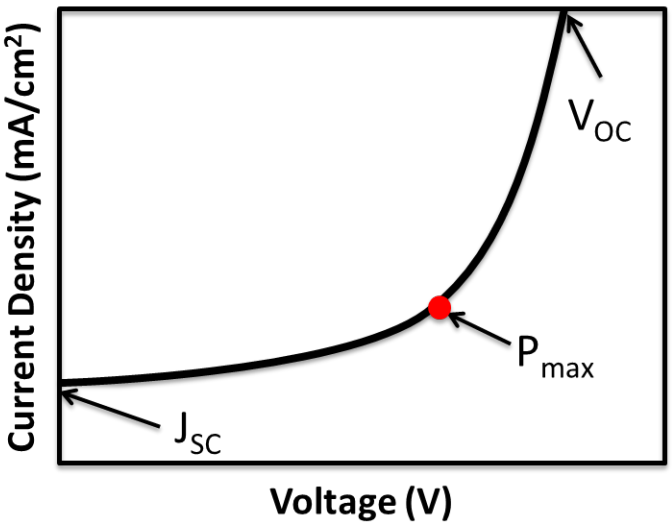

Figure 1-3. A cartoon example of what device power output curves look like. The upper-left corner is taken as the origin.

Under illumination, at zero voltage a current is generated which is referred to as short-circuit current (J_{SC}). As voltage is increased, eventually a point is reached where no current is measured across the device, denoting the open-circuit voltage (V_{OC}). Because power is equal to current times voltage, we can assign a maximum power point to the curve (P_{max}), whose product is referred to as fill factor (FF). PCE is calculated using the three aforementioned device metrics and the power of the incident light (P_{in}) according to Equation 1-1:

Equation 1-1: $$PCE = \frac{J_{SC} \times V_{OC} \times FF}{P_{in}}$$

The J_{SC} is limited by how many photons are absorbed (i.e. how many charge carriers are generated), and how efficiently charge carriers can transport through the bulk. The V_{OC} value is related to the difference in energy between the HOMO of the donor material and the LUMO of the acceptor. Together these values form the basis of modern molecular design strategies. However, it is of the utmost importance to remember that Equation 1.1 does not reflect the importance of interfaces or morphology, which will be explored necessarily in more detail chapters II and III, respectively.

C. Design Rules for Donor Materials

Small molecules present some key advantages over polymers with respect to molecular design. One notorious challenge associated with the preparation of polymers is the reproducibility of the size and distribution of molecular weight – a caveat of the step-growth polycondensation reactions that efficiently deliver high molecular weight polymers. This gives rise to an additional challenge with respect to molecular design; structural modifications to repeat units targeted toward tailoring material properties can affect the size and distribution of molecular weight of the product. The variation of molecular dimensions convolutes the relationship between structural modifications and bulk properties. Small molecules, however, are virtually insensitive to these issues. While they remain sensitive to impurities,[22] their inherently smaller size allows for a wider selection of purification and characterization techniques.[23-26] Using design principles established by the polymer

community, a class of molecules was developed that broadened the landscape of OPV materials research.

Conjugated small molecules described here adhere to a simple modular framework of discreet conjugated units that can be coupled using well-known, high-yielding organic coupling reactions. The scaffold consists of a relatively electron-rich core (D) with solubilizing side groups flanked by two relatively electron poor units (A), and terminates with a conjugated end-cap unit (D') also bearing side groups, i.e. D'ADAD' (Figure 1.4).[27] Each component influences the final molecule's electronic, optical and physical properties, providing multiple opportunities to tune each of the aforementioned parameters. By employing well-studied conjugated building blocks, this study took the first step in fully understanding the function imparted by each structural unit. This particular study exclusively used pyridyl[2,1,3]thiadiazole heterocycle as the acceptor fragment. Beyond its useful electron deficient nature, the pyridyl nitrogen endows asymmetric reactivity to the dibrominated analog, enabling mono-functionalization.[28-30] Overall, this platform delivers facile synthetic entry to an array of molecules that can be directly compared for qualitative design principles as a function of structural modification.

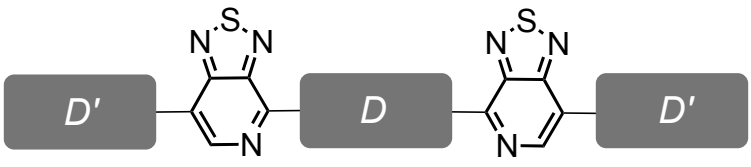

Figure 1-4. The D'ADAD' architecture with pyridyl[2,1,3]thiadiazole in the "A" position.

By using a single acceptor fragment, different donor units can be assigned a relative donor "strength" as evidenced by variation in electrochemical and optical properties. A donor unit is described as stronger than another if it yields a reduction (closer to vacuum) in ionization potential (IP), as well as a lower energy charge transfer transition for the resulting chromophore. Since the IP reflects the energy of the highest occupied molecular orbital (HOMO), this is a critical tool, in that this value sets an upper limit to the V_{OC}. Simultaneously, a shift in IP that favors larger V_{OC} values concomitantly widens the bandgap, setting a higher energy threshold for photon absorption, resulting in fewer photons being absorbed. It is important to remember that no single property is affected in structural modifications. In this case core donor fragment changes also impact melting points without any observable correlation, but varying the length and/or branching of solubilizing side groups afford some fine control. The relationships described so far hold true for terminal fragments as well, but smaller changes to optical and electronic properties can be accessed simply, by changing the length of the end cap. Ultimately, in generating this matrix structure and property changes led to the development of p-DTS$(PTTh_2)_2$ (**1-1**, Figure 1.5) which represented a paradigm shift in small-molecule organic BHJ solar cells.

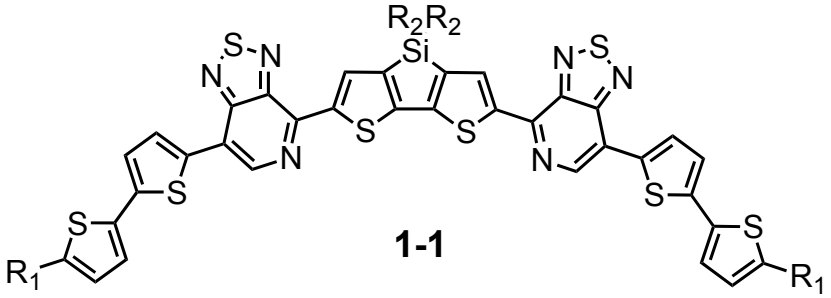

1-1

Figure 1-5. Chemical structure of molecule **1-1**. R_1 = hexyl and R_2 = 2-ethylhexyl.

In a standard device architecture with $PC_{71}BM$, molecule **1-1** demonstrated an optimized PCE value of 6.7 %, more than 50 % higher than the preceding highest reported value.[16] Unfortunately, a high-performing molecule does not make a useful technology. The optimized OPV device with molecule **1-1** serving as the donor utilized molybdenum oxide as an anode interlayer. Molybdenum oxide layers are deposited via thermal evaporation, necessitating high temperatures and low pressures only accessible with costly specialized equipment. Many devices utilize poly(3,4-ethylenedioxythiophene poly(styrenesulfonic acid) (PEDOT:PSS) to serve the same purpose. The key advantage is that PEDOT:PSS can be cast from a suspension in water, and high-throughput production generally favors solution processability; however, molecule **1-1** exhibits diminutive performance in devices using PEDOT:PSS. The next chapter describes how we elucidated the chemistry at this interface and our molecular design strategy to enable utility of high-performance molecular donors on solution-processable substrates.

D. References

(1) Brabec, C. J.; Sariciftci, N. S.; Hummelen, J. C. *Advanced Functional Materials* **2001**, *11*, 15.

(2) Morel, D. L.; Ghosh, A. K.; Feng, T.; Stogryn, E. L.; Purwin, P. E.; Shaw, R. F.; Fishman, C. *Applied Physics Letters* **1978**, *32*, 495.

(3) Thompson, B. C.; Fréchet, J. M. J. *Angewandte Chemie International Edition* **2008**, *47*, 58.

(4) Perez, L. A.; Chou, K. W.; Love, J. A.; van der Poll, T. S.; Smilgies, D. M.; Nguyen, T. Q.; Kramer, E. J.; Amassian, A.; Bazan, G. C. *Advanced materials* **2013**, *25*, 6380.

(5) Jakubka, F.; Heyder, M.; Machui, F.; Kaschta, J.; Eggerath, D.; Lövenich, W.; Krebs, F. C.; Brabec, C. J.; Jakubka, F.; Heyder, M.; Machui, F.; Kaschta, J.; Eggerath, D.; Lövenich, W.; Krebs, F. C.; Brabec, C. J. *Solar Energy Materials & Solar Cells* **2013**, *109*, 120.

(6) Krebs, F. C. *Solar Energy Materials and Solar Cells* **2009**, *93*, 394.

(7) Yu, G.; Gao, J.; Hummelen, J. C.; Wudl, F.; Heeger, A. J. *Science* **1995**, *270*, 1789.

(8) Liu, T.; Troisi, A. *Advanced materials* **2013**, *25*, 1038.

(9) Tsao, H. N.; Cho, D. M.; Park, I.; Hansen, M. R.; Mavrinskiy, A.; Yoon, D. Y.; Graf, R.; Pisula, W.; Spiess, H. W.; Müllen, K. *Journal of the American Chemical Society* **2011**, *133*, 2605.

(10) Zhang, W.; Smith, J.; Watkins, S. E.; Gysel, R.; McGehee, M.; Salleo, A.; Kirkpatrick, J.; Ashraf, S.; Anthopoulos, T.; Heeney, M.; McCulloch, I. *Journal of the American Chemical Society* **2010**, *132*, 11437.

(11) Bijleveld, J. C.; Gevaerts, V. S.; Di Nuzzo, D.; Turbiez, M.; Mathijssen, S. G. J.; de Leeuw, D. M.; Wienk, M. M.; Janssen, R. A. J. *Advanced materials* **2010**, *22*, E242.

(12) Bijleveld, J. C.; Zoombelt, A. P.; Mathijssen, S. G. J.; Wienk, M. M.; Turbiez, M.; de Leeuw, D. M.; Janssen, R. A. J. *Journal of the American Chemical Society* **2009**, *131*, 16616.

(13) Bijleveld, J. C.; Shahid, M.; Gilot, J.; Wienk, M. M.; Janssen, R. A. J. *Advanced Functional Materials* **2009**, *19*, 3262.

(14) Zhang, M.; Tsao, H. N.; Pisula, W.; Yang, C.; Mishra, A. K.; Müllen, K. *Journal of the American Chemical Society* **2007**, *129*, 3472.

(15) van der Poll, T. S.; Love, J. A.; Nguyen, T. Q.; Bazan, G. C. *Advanced materials* **2012**, *24*, 3646.

(16) Sun, Y.; Welch, G. C.; Leong, W. L.; Takacs, C. J.; Bazan, G. C.; Heeger, A. J. *Nat Mater* **2012**, *11*, 44.

(17) Zhao, L.; Zhao, S.; Xu, Z.; Gong, W.; Yang, Q.; Fan, X.; Xu, X. *Appl. Phys. A* **2014**, *114*, 1361.

(18) Peters, R.; Dalnoki-Veress, K. *Eur. Phys. J. E* **2012**, *35*, 1.

(19) Li, G.; Shrotriya, V.; Huang, J.; Yao, Y.; Moriarty, T.; Emery, K.; Yang, Y. *Nat Mater* **2005**, *4*, 864.

(20) van Duren, J. K. J.; Yang, X.; Loos, J.; Bulle-Lieuwma, C. W. T.; Sieval, A. B.; Hummelen, J. C.; Janssen, R. A. J. *Advanced Functional Materials* **2004**, *14*, 425.

(21) Yang, X.; Loos, J. *Macromolecules* **2007**, *40*, 1353.

(22) Leong, W. L.; Welch, G. C.; Kaake, L. G.; Takacs, C. J.; Sun, Y.; Bazan, G. C.; Heeger, A. J. *Chemical Science* **2012**, *3*, 2103.

(23) Walker, B.; Kim, C.; Nguyen, T.-Q. *Chemistry of Materials* **2010**, *23*, 470.

(24) Li, Y.; Guo, Q.; Li, Z.; Pei, J.; Tian, W. *Energy & Environmental Science* **2010**, *3*, 1427.

(25) Roncali, J. *Accounts of Chemical Research* **2009**, *42*, 1719.

(26) Riede, M.; Mueller, T.; Tress, W.; Schueppel, R.; Leo, K. *Nanotechnology* **2008**, *19*, 424001.

(27) Welch, G. C.; Perez, L. A.; Hoven, C. V.; Zhang, Y.; Dang, X.-D.; Sharenko, A.; Toney, M. F.; Kramer, E. J.; Nguyen, T.-Q.; Bazan, G. C. *Journal of Materials Chemistry* **2011**, *21*, 12700.

(28) Handy, S. T.; Wilson, T.; Muth, A. *J Org Chem* **2007**, *72*, 8496.

(29) Schroter, S.; Stock, C.; Bach, T. *Tetrahedron* **2005**, *61*, 2245.

(30) Tilley, J. W.; Zawoiski, S. *J Org Chem* **1988**, *53*, 386.

II.Non-Basic Small Molecule Donor for Utility on Solution Deposited Substrates

The small molecule **2-2** is designed for incorporation into solution-fabricated high-efficiency organic solar cells. Of primary importance is the incorporation of electron poor heterocycles that are not prone to protonation and thereby enable the incorporation of commonly used interlayers between the organic semiconductor and the charge collecting electrodes. These features have led to the creation of **2-2**/$PC_{71}BM$ solar cells with power conversion efficiencies of up to 7%.

A. Introduction

As described in the previous chapter, small-molecule bulk-heterojunction organic photovoltaics have become a competitive alternative to the more widely studied conjugated polymer based counterparts.[1-4] Potential advantages offered by molecular systems are that they are monodisperse in nature and, due to having a higher solubility than polymeric analogs, can be purified and characterized using standard organic chemistry protocols. Modifications can also be made to molecular frameworks to fine-tune properties, without convolution arising from average molecular weight variations and polydispersities.[5,6] The development and device optimization of molecule **1-1** demonstrated that solution processed molecular solar cells can access high efficiencies, comparable to that of narrow band gap conjugated polymers.[7] Unfortunately high-performance of this system is limited to thermally evaporated substrates in spite of readily available solution-processed alternatives, i.e.

PEDOT:PSS. Closer scrutiny of the fragments comprising **1-1** reveal that when in contact with PEDOT:PSS, interfacial chemistry can occur resulting in protonated species that diminish overall device performance. We first consider that the success of this architecture has largely hinged on the inclusion of [1,2,5]-thiadiazolo-[3,4-c]-pyridine heterocyle (also known as pyridyl[2,1,3]thiadiazole and here abbreviated as PT), which can be described as an electron deficient unit.[8] Coupling PT to other readily available conjugated building blocks affords chromophores with desirable light harvesting properties.[9] Another useful quality associated with PT is that the pyridyl nitrogen imparts asymmetry such that near quantitative site-selective cross-coupling can be achieved by using the 4,7-dibromo-[1,2,5]thiadiazolo[3,4-*c*]pyridine precursor.[10-13] and this reactivity is relevant to the synthesis of **1-1**. This asymmetric reactivity can be rationalized by considering the electron withdrawing power of nitrogen from carbon. It stands to reason that any amount of localized positive charge on the carbon adjacent to the pyridyl nitrogen will stabilize oxidative addition in a catalytic cycle (Figure 2-1). In combination with $PC_{71}BM$, **1-1** makes solar cells with a power conversion efficiency (PCE) upwards of 6.7 %.

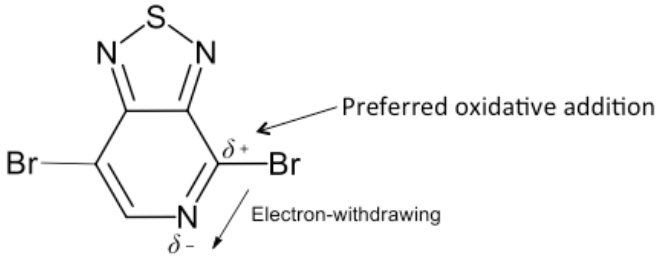

Figure 2-1. An indication of the partial positive charge on carbon-4 inducing preferential oxidative addition.

As noted, **1-1**/$PC_{71}BM$ blends yield high PCEs in device architectures that employ metal oxides, i.e. molybdenum oxide, as an anode interlayer. Using the more widely used poly(3,4-ethylenedioxythiophene):poly(styrenesulfonicacid) (PEDOT:PSS) interlayer leads to a diminished performance, and in particular a loss in open circuit voltage (V_{OC}).[14,15] This drop in performance has been attributed to the acidic nature of PEDOT:PSS, which ultimately results in protonation of the PT pyridyl nitrogen.

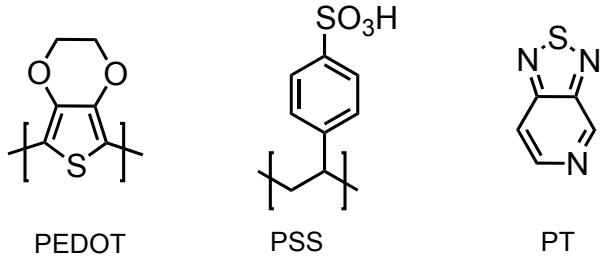

Figure 2-2. Chemical structure of PEDOT, PSS and the PT fragment.

This follows logically from previous work, where it was shown that the pyridyl nitrogen in the chromophore back bone can act as a lewis-basic site, where lewis acids can bind and manipulate charge transfer properties, both in the case of absorption and emission.[16,17] More sophisticated explanations has been offered specifically addressing the consequences of the interface between pyridyl containing species and (PEDOTT:PSS).[14,15] The first study finally showed explicit evidence of a chemical interaction between a regioisomer of **1-1** (**2-1**, Figure 2-3) and acidic protons from PEDOT:PSS by looking at changes in absorption in thin films.

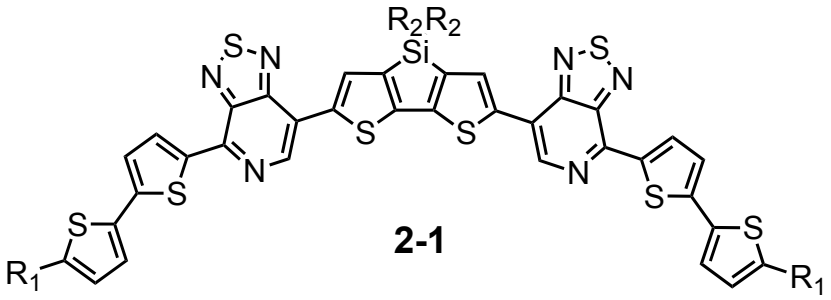

Figure 2-3. Chemical structure of molecule **2-1**. R_1 = hexyl and R_2 = 2-ethylhexyl

Shown in Figure 2-4 are three absorption spectra that compare films of molecule **2-1** as a function of film thickness, underlying substrate, and with and without tosylic acid. In figure 2-4a and 2-4b, neat films of **2-1** were cast from a 0.2 wt% and 0.01 wt% solutions, respectively. Unsurprisingly, the thicker films, cast from the solution of higher concentration, show no notable differences. But the thinner film cast on PEDOT:PSS exhibits a distinct bathochromic shift in the onset of absorption. To eliminate the possibility of this change being a morphological phenomenon, films were also cast with the analogous Brønsted acid, tosylic acid, and indeed, the same effect is achieved. The similarity suggests it is the presence of a protic acid that gives rise to the absorption shift.

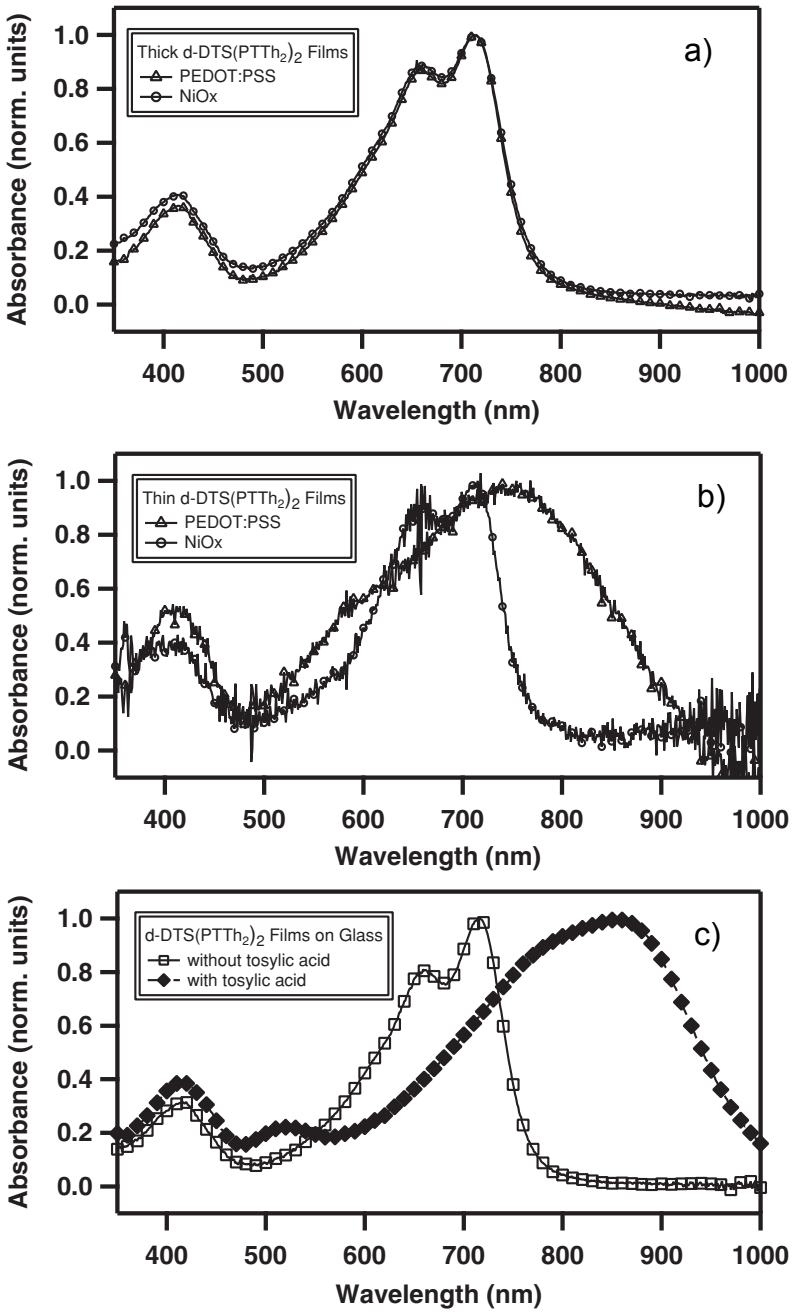

Figure 2-4. Normalized thin film absorption spectra of **2-1** cast from a) 0.2 wt% b) 0.01 wt% solutions on PEDOT:PSS and nickel oxide and c) on glass with and without tosylic acid.

The shift in absorption can be rationalized by considering the nature of the parent chromophore. Having relatively electron-rich and electron-poor portions of the conjugated backbone stabilizes charge transfer characteristics. PT is already an electron-poor fragment, and protonation installs a localized positive charge. Therefore, the protonated species is expected to exhibit further stabilization and ultimately lower energy transitions. X-ray photoelectron spectroscopy (XPS) confirms the locality of this effect via changes to the nitrogen 1s electron binding energy as shown in Figure 2-5.

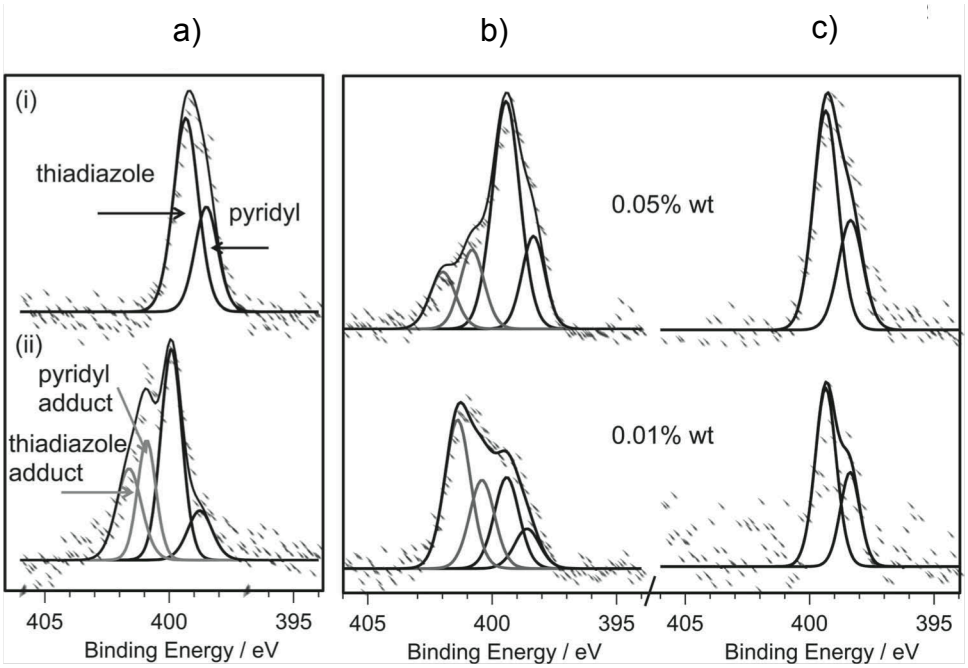

Figure 2-5. XPS of core level N 1s levels of **2-1**. Films were cast on a) gold, b) PEDOT:PSS, and c) nickel oxide. Spectra are shown i) before and ii) after exposure to tosylic acid.

In a subsequent study using ultraviolet photoelectron spectroscopy (UPS) and XPS, it was determined that the protonated form of p-DTS($PTTh_2$)$_2$ ultimately behaves as an entirely different semiconducting species with a different ionization potential. The result is a population of interfacial charge extraction barriers due to local increases in work function. This ultimately limits the available options for interfacial layers, specifically precluding the use of PEDOT:PSS, a ubiquitous and solution-processable material. The need to develop materials with versatile utility that will not limit fabrication options led us to design a molecule with desirable optical, electronic and physical properties without the incorporation of sites sensitive to protonation. Indeed, as shown below this evolution in molecular design makes it possible to fabricate devices that achieve PCE values up to 7 % using PEDOT:PSS as the interfacial layer, thereby opening a wider range of options for device fabrication.

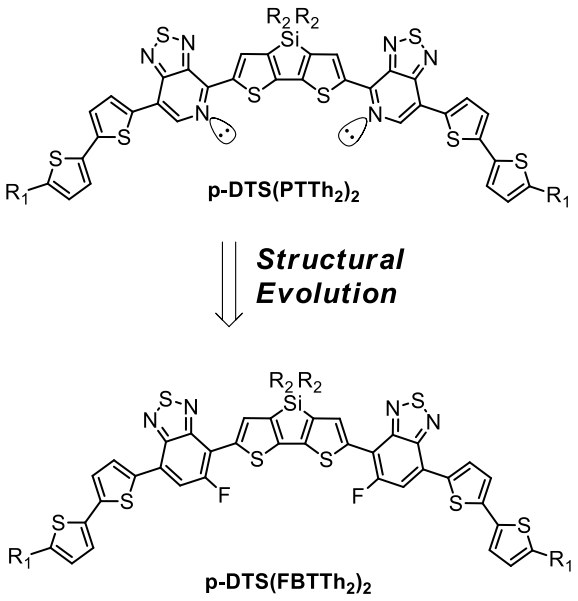

Figure 2-6. Chemical structures of **1-1** and **2-2**. R_1 = n-hexyl R_2 = 2-ethylhexyl.

As shown in Figure 2-6, the target of our studies is 7,7'-(4,4-bis(2-ethylhexyl)-4H-silolo[3,2-b:4,5-b']dithiophene-2,6-diyl)bis(6-fluoro-4-(5'-hexyl-[2,2'-bithiophen]-5-yl)benzo[*c*][1,2,5]thiadiazole) (**2-2**). A key feature of this chromophore is the incorporation of 5-fluorobenzo[c][1,2,5]thiadiazole (FBT, compound **3** in Scheme 2-1) as the acceptor unit in place of the previously described PT. FBT has previously found utility in organic polymers for high performance OPV devices.[18,19] The key distinction between FBT and similar building blocks is that the fluorine atom provides an electron-withdrawing functionality with no lone pairs of electrons that may be prone to participate in acid/base reactions.[20-22] This electron withdrawing effect increases the electron deficiency of the heterocycle compared to the hydrogen substituted equivalent. In addition, the fluorine atom

changes the reactivity of the two bromide functionalities in 4,7-dibromo-5-fluorobenzo[*c*][1,2,5]thiadiazole ($FBTBr_2$)[23] much like the previously described PT nitrogen, which allows for facile synthetic access to the desired structure.

B. Synthesis We offer two synthetic routes to **2-2**. Protocols for preparing organic semiconductors tend to rely on organometallic cross-coupling procedures such as the Stille reaction, wherein trialkyl stannanes are couples to organohalides. Given its efficiency and versatility, the Stille serves as a logical option for the preparation of the presented molecules. The details of this route are described in the subsequent sub-section. In the interest of reducing both economic and environmental costs, direct heteroarylation chemistry eliminates the need to prepare and use tin reagents, which require both trialkyltin halides and highly pyrophoric butyllitium reagents. A milder alternative synthetic route is offered in the sub-section following the Stille-centric pathway. This effort was a side project not central to addressing interfacial issues for molecule **1-1**. To continue with characterization of **2-1**, the reader is directed to part C of this chapter.

1. Preparation of **2-2** using Stille cross-coupling.

The synthesis of p-DTS($FBTTh_2$)$_2$ is shown in Scheme 2-1. All materials are either commercially available or easily prepared. Starting with 4-fluoro-1,2-benzenediamine (**1**), formation of the thiadiazole ring can be achieved by refluxing with thionyl chloride and triethylamine in chloroform to afford **2**. Compound **2** is then subjected to bromine in 48 % HBr at 128 °C for two days to afford **3**.

Dibromide **3** is coupled to the stannylated dithiophene fragment **4** under Stille conditions to afford compound **5**. A critical observation in the course of optimizing this protocol was that **5** and residual amounts of **3** elute at the same rate in column chromatography conditions. Prior to this realization, the presence of **3** in the subsequent step resulted in the generation of extended oligomers due to the presence of both a dibromide and a distannane. Even trace amounts of impurities in the bulk can drastically diminish the performance of devices.[24] An effective solution to this problem is sublimation of residual amounts of **3** from **5**. The regiochemistry of the fluorine atom with respect to the dithiophene fragment was confirmed by 2D ^{1}H-^{1}H NOE NMR spectroscopy (see experimental and supplementary information section). Compound **5** is then coupled to the distannylated cyclopentadithiophene (**6**) to afford **2-2**. Full experimental details can be found in the experimental and supplementary information section at the end of the chapter.

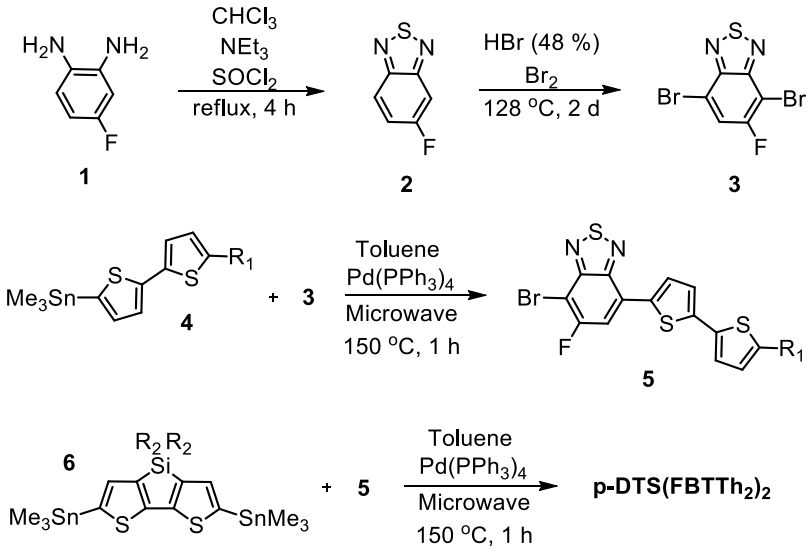

Scheme 2-1. Synthetic scheme towards p-DTS(FBTTh$_2$)$_2$. R_1 = n-hexyl R_2 = 2-ethylhexyl. Full synthetic details are available in the Supporting Information.

2. Alternative Synthetic Route: Direct Heteroarylation Methodologies.

In order to push organic photovoltaics towards a realistic alternative energy option, it is important to consider a systems perspective. Specifically, strictly focusing on strategies to control material properties only offers gains in improving the efficiency of devices; there is an additional cost that comes with the preparation of materials. To that end, there are many literature reports that address the costly nature of forming aryl-aryl bonds [refx]. Direct heteroarylation aims to remove the necessity of toxic, costly or dangerous reagents and conditions such as butyllithium or trialkyl stannanes, and in turn the resulting hazardous by-products. The scope of these efforts is wide and expanding.[25-34]

A report from Scherf and coworkers described the preparation of a copolymer comprising cyclopenta[2,1-b:3,4- b']dithiophene (CDT) and benzo[2,1,3]thiadiazole (BT) (Scheme 2-2a). This transformation bears similarity to multiple pairs of coupling partners in scheme 2-1, and are highlighted in Scheme 2-2. Redundant steps are omitted for clarity. Parameters like molecular weight and polydispersity may convolute the interpretation of reaction efficiency, but this served as a logical reference point upon which to build a synthetic scheme.

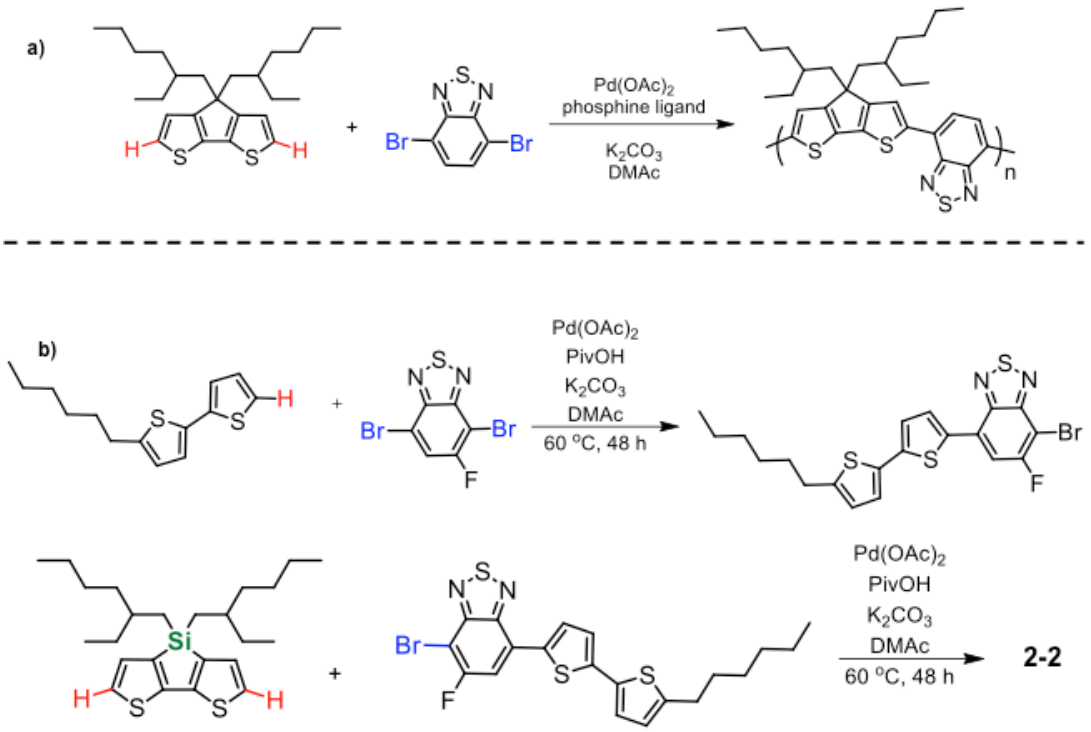

Scheme 2-2. a) Reported reaction conditions for direct heteroarylation and b) analogous coupling partners in preparation of **2-2**. Bromine and hydrogen reactive sites indicated in blue and red, respectively.

In accordance with the architecture described in chapter 1, the first step in Scheme 2-2b couples a hexyl bithiophene end cap with the FBT acceptor to afford what can be described as a molecular wing fragment with a yield of 79 %. This wing can then be coupled to the donor core using the same conditions to afford **2-2** with 35 % yield. While the former step offers a superior yield to the Stille coupling, the latter is significantly less efficient. Considering strictly the aryl-aryl bond formation steps, overall yields for the Stille and direct heteroarylation routes are 36 and 28 %,

respectively. While inferior in efficiency, direct heteroarylation promises gains in avoiding costly, hazardous, and environmentally harmful reagents and conditions.

C. Characterization

Material properties were investigated using solution and thin film UV-visible absorption, cyclic voltammetry, thermogravimetric analysis and differential scanning calorimetry. Here we present key data relevant to device incorporation. Details are available in the experimental and supplementary information section. Where appropriate, we include data for molecule **1-1** for comparison.

Optical properties were investigated using UV-visible absorption spectroscopy (Figure 2-7a). In chloroform **2-2** exhibits a broad low energy transition with favorable overlap with the solar spectrum, with a λ_{max} value of 590 and λ_{onset} value of 670 corresponding to an optical band gap of 1.85 eV. This band gap is wider than one might expect compared to **1-1**, which from solution absorption possesses a band gap of 1.73 eV. We speculate that the presence of fluorine atoms ortho to aryl-aryl bonds may induce and increased dihedral angle and disrupt conjugation. Films were prepared by spin-casting a 0.2 wt% solution in chloroform onto glass substrates. In the solid state, **2-2** exhibits a bathochromically shifted low energy transition with a λ_{max} value of 678 nm and λ_{onset} value of 800 nm, corresponding to an optical band gap of 1.55 eV. Thin film absorption exhibits vibronic structure, typical of ordered thin films.[35,36] The λ_{max} red-shift of 88 nm in going from solution to the solid is notably higher compared to **1-1**, in which the λ_{max} red shift is 55 nm. If the earlier

assumption that the fluorine atoms could cause the conjugation to be interrupted were true, this difference could be attributed to the molecular backbone planarizing upon condensation.

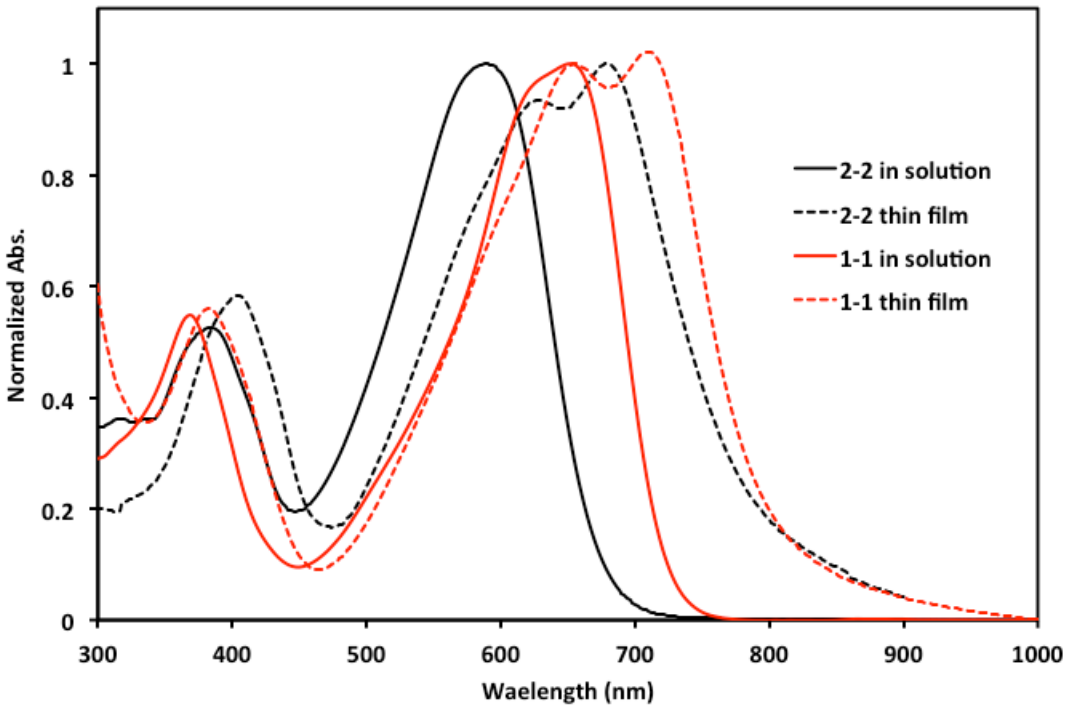

Figure 2-7. Absorption spectra of **2-2** and **1-1** solutions in chloroform and thin film.

Solution cyclic voltammetry (CV) measurements indicate that the highest occupied molecular orbital (HOMO) and lowest unoccupied molecular orbital (LUMO) are -5.12 and -3.34 eV, respectively, corresponding to a band gap of 1.78 eV, in reasonable agreement with the optical band gap calculated from solution absorption onset.[37] These data suggest that the frontier molecular orbitals of **2-2** line up favorably with those of common fullerene acceptors to generate useful V_{OC} in

BHJ solar cells.[38,39] Table 2-1 provides a concise summary of the characterization data for **1-1** and **2-2**.

Table 2-1. Side-by-side comparison of characterization data for **2-2** and **1-1**.

		2-2	**1-1**
Solution	λ_{max} ***(nm)***	590	655
	λ_{onset} ***(nm)***	670	715
	E_{gap} ***(eV)***	1.85	1.73
Film	λ_{max} ***(nm)***	678	710
	λ_{onset} ***(nm)***	800	815
	E_{gap} ***(eV)***	1.55	1.52
E. Chem.	***HOMO (eV)***	-3.34	-3.6
	LUMO (eV)	-5.12	-5.2
	gap (eV)	1.78	1.6
Thermal	***Tm (°C)***	208	209
	Tc (°C)	116	168
	T_d ***(°C)***	421	415

To probe whether the design elements proved useful to reduce sensitivity toward protonation, the solution absorption profile of **2-2** was monitored as function of CF_3CO_2H concentration. Figure 2-8a shows that the absorption of **2-2** remains unchanged when in the presence of up to ten equivalents of CF_3CO_2H. For comparison, **2-1** was subjected to the same conditions as a control. The resulting absorption profiles (Figure 2-8b) show significant changes immediately upon acid addition; namely one observes new low energy transitions suggesting that the chromophore backbone is influenced by the protonation. Notably, the effect does not saturate even up to ten equivalents suggesting equilibrium exists between protonated and non-protonated species in solution. These data indicate that **2-2** is more resilient against acidic conditions and argues in favor of using PEDOT:PSS interlayers in

OPV devices. The true test of this resilience follows, in the form of device optimization.

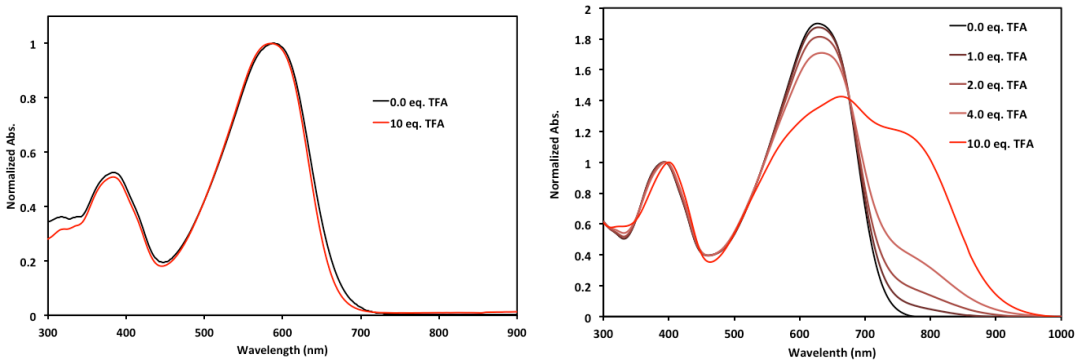

Figure 2-8. Solution absorption of a) **2-2** and b) **2-1** as a function of trifluoroacetic acid (TFA) concentration.

Photovoltaic devices were fabricated using the general architecture: ITO/PEDOT:PSS/**2-2**:$PC_{71}BM$/Ca/Al. Solutions were cast from a 3.5 % w/v total blend concentration in chlorobenzene. A series of studies were conducted to explore improvements in PCE. The influence of the **2-2**:$PC_{71}BM$ ratio was examined by looking at the following compositions: 40:60, 50:50, 60:40 and 70:30. Spin-rates ranging from 1000 rpm to 5000 rpm were also examined. We note that films of **2-2** and $PC_{71}BM$ formed smooth films when cast atop PEDOT:PSS, with rms < 2.0 nm, as confirmed by atomic force microscopy (Experimental and supplementary information). Best devices from this examination had a **2-2**:$PC_{71}BM$ ratio of 60:40, as produced by spin coating at 1750 rpm; typical current-voltage characteristics and external quantum efficiency (EQE) plots are shown in Figure 2-9. These data show a

PCE of 1.8%, with a V_{OC} of 780 mV, a short circuit current (J_{SC}) of 6.6 mA cm^{-2}, and a fill factor (FF) of 0.36. Post-deposition annealing temperatures were then investigated on the films described above by looking at the effect of heating for 10 minutes within the temperature range of 70 to 150 °C. The best improvement was observed by heating at 130 °C: V_{OC} = 820 mV, J_{SC} = 10.8 mA cm^{-2}, and FF = 0.65, yielding a PCE of 5.8%.

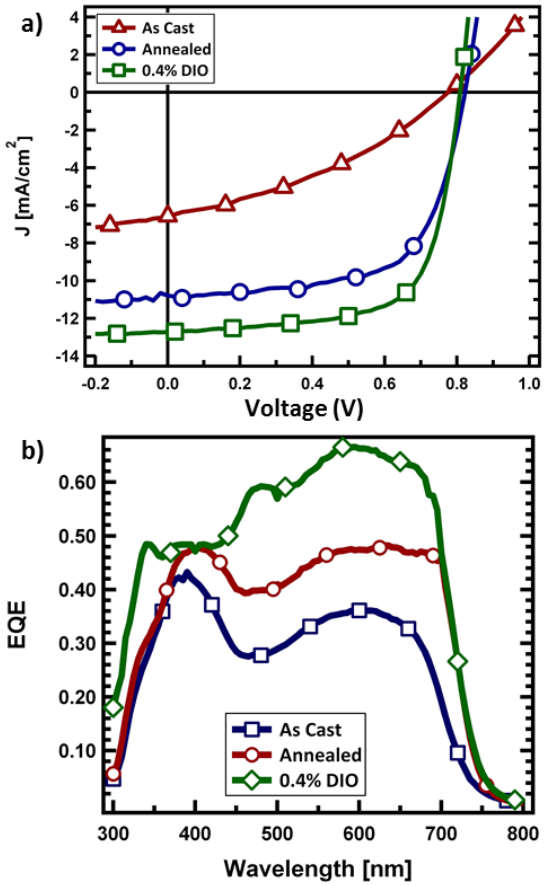

Figure 2-9. a) Current voltage characteristics of solar cells with an active layer comprised of **2-2** and $PC_{71}BM$ as cast, annealed and with 0.4 % (v/v) diiodooctane solvent additive. b) Corresponding external quantum efficiency plots.

Further optimization involved using small quantities of diiodooctane (DIO) as a solvent additive during the film-casting step. This strategy has been shown to influence film formation, providing a handle to manipulate morphology and increase device performance. The following DIO concentrations in chlorobenzene were used: 0.1, 0.15, 0.2, 0.25, 0.3, 0.35, 0.4, 0.5, 1.0 v/v %. One finds a progressive increase in PCE up to [DIO] = 0.4 v/v %, followed by a rapid deterioration of device characteristics. Altogether, we find that by using [DIO] = 0.4 v/v %, followed by heating at 70 ˚C (in order to remove residual solvent and DIO), one can obtain a PCE of 7.0% (V_{OC} = 809 mV, J_{SC} = 12.8 mA cm^{-2}, and FF = 0.68), which at the time of publication was the highest reported efficiency of a solution processed SM-BHJ solar cell to date. The optimized fabrication conditions for **1-1** entail a similar blend ratio and a [DIO] of 0.25 v/v %, corroborating the targeted consistency in material properties between **1-1** and **2-2**. From the EQE spectra in Figure 3b, the most important enhancement in the photocurrent occurs in the low energy region, attributed to excitons generated on **2-2**.[40,41] It is worth noting that a FF of 0.68 is uncommonly high for SM-BHJ solar cells, suggesting highly efficient charge extraction.[42]

D. Morphological Considerations

Device metrics alone do not explain the effect of post-deposition annealing or casting solvent additives. In subsequent studies using transmission electron microscopy (TEM) and *in-situ* grazing-incidence wide-angle x-ray scattering (GIWAXS) we gained a clearer picture of BHJ morphology and film-formation, respectively.[43,44]

Figure 2-10 shows TEM images of **2-2**:$PC_{71}BM$ blend films a) as-cast, b) annealed, and with c) 0.4 and d) 1.0 v/v % DIO solvent additive. As-cast films appear featureless, but post-deposition annealing and solvent additive clearly induce the formation the formation of well-defined wire-like domains. In the annealed films contain long wires with a characteristic width of approximately 40-50 nm. With additive a continuous network forms with grains sizes on the order of 30-40 nm. With high additive concentration substantially larger domains appear that are microns long and up to 100nm thick. Based on the limitation of exciton diffusion it follows intuitively that the small ordered domains associated with the optimized additive-processed film also exhibit the highest performance.

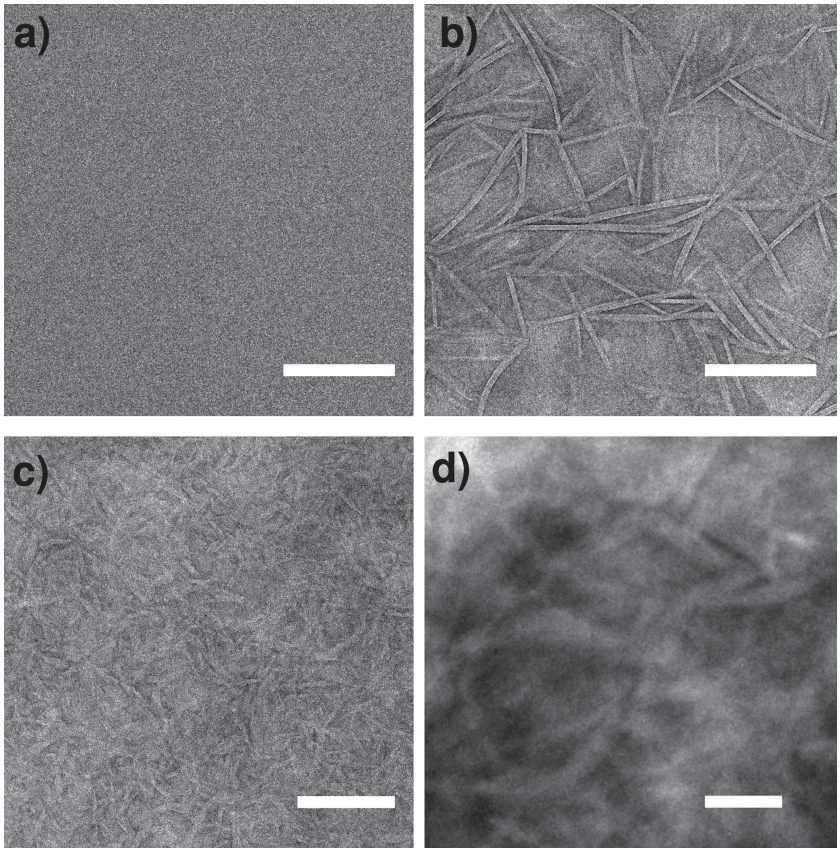

Figure 2-10. Bright field TEM images of **2-2**:$PC_{71}BM$ blend films a) as-cast, b) annealed, and with c) 0.4 and d) 1.0 v/v % DIO solvent additive.

One limitation of TEM is the 2-dimensional nature of the output images. Features shown in Figure 2-10 could potentially be surface features. For a perspective on depth, cross-sectional TEM was also used (Figure 2-11). The same features described previously appear here, and traverse much of the bulk.

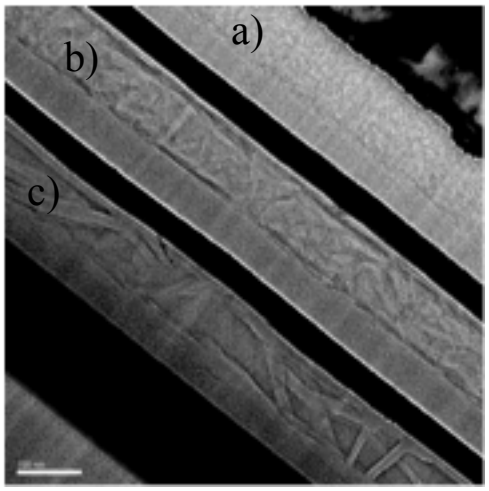

Figure 2-11. Cross-sectional TEM images of **2-2**:$PC_{71}BM$ blend films a) as-cast, b) with 0.4 v/v % DIO solvent additive, and c) annealed.

More recently, a dynamic perspective was gained on the role of processing additives in film formation by looking at GIWAXS during spin-casting. Plots shown in Figure 2-12 are azimuthal integrations of scattering plots as a function of time with and without solvent additive. In both cases, it takes approximately five seconds for a stable scattering peak to appear, as evidenced by the abrupt appearance of peaks.

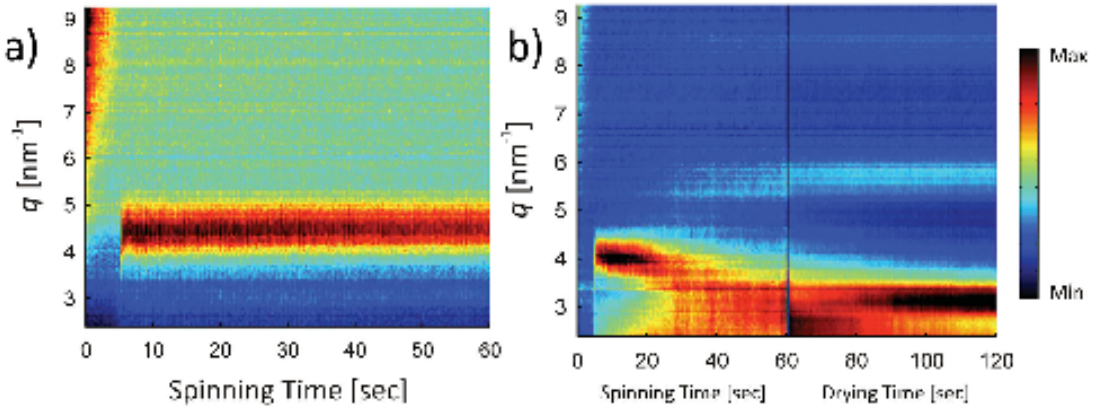

Figure 2-12. *In-situ* GIWAXS plots of **2-2**:$PC_{71}BM$ blends during spin-casting a) without and b) with solvent additive.

Without additive, a single peak appears and remains unchanged for the duration of the drying process; however, with DIO as a solvent additive the peak that forms at five seconds attenuates over 30-60 seconds, and a new scattering profile develops significantly different from the non-additive case. Three main effects can be attributed to processing **2-2**:$PC_{71}BM$ with DIO from the *in-situ* GIWAXS measurements: 1) the formation of a metastable intermediate phase of **2-2** during the initial 20 s of the spin-casting process, which is different from that of the final structure of the film and of the film processed without additive; 2) the structure of the film formed in the presence of additive continues to evolve and gradually transforms into the final structure over the next 60–70 s of the spin casting and drying process (by contrast, the non-additive treated solution leads to rapid formation of a static, kinetically trapped structure, which does not evolve further

once the film is formed in the first 5–10 s of the spin-casting process); and 3) both the metastable and final structures formed in the presence of additive have more intense and narrower peaks.

E. Conclusions

The inclusion of the PT heterocycle into a conjugated backbone imposes sensitivity of semiconducting properties to acidic environments by virtue of an in-chain pyridyl nitrogen. The role of this heteroatom is to enhance acceptor character of the fragment and grants the added benefit of asymmetric reactivity, suggesting alternative electron withdrawing functional groups could offer the same advantages without unwanted reactivity. Our new molecular donor, **2-2**, was designed and synthesized with favorable properties for light harvesting and enhanced stability toward commonly used acidic interlayers. This material was also used successfully to fabricate one of the highest performance solution-processed molecular BHJ solar cells reported to date. This high-performance platform also presented an opportunity to explore the role of processing additives in unprecedented detail. The **2-2** architecture implements a CF group as an inert electron-withdrawing functionality, and exhibits similar properties to **1-1**. It is reasonable that this strategy can be applied to other molecular systems to improve stability and enable greater options for device fabrication.

F. Experimental and Supplementary Information

General Details: Preparations were carried out on a bench top or under an

atmosphere of dry, O_2-free N_2 employing both Schlenk line techniques and a Vacuum Atmospheres inert atmosphere glove box. Deuterated chloroform ($CDCl_3$) was purchased from Cambridge Isotopes Laboratory and used as received. All reactants and reagents are commercially available and used as received, unless otherwise noted.

General Synthesis: Compound 5,5'-bis(trimethylstannyl)-3,3'-di-2-ethylhexylsilylene-2,2'-bithiophene ($DTS(SnMe_3)_2$) and 5'-hexyl-2,2'-bithiophene-5-trimethylstannane were prepared by methods similar to those reported in the literature.[6]

NMR Spectroscopy: ^1H and ^{13}C nuclear magnetic resonance (NMR) spectroscopy spectra were recorded on a Varian VNMRS 600 MHz Spectromenter at 25°C unless otherwise noted. ^1H and ^{13}C NMR spectra are referenced to SiMe4 using the residual solvent peak impurity of the given solvent. Chemical shifts are reported in ppm and coupling constants in Hz as absolute values. 2D NOE ^1H-^1H correlation experiments were completed on a Bruker Avance-500 MHz spectrometer at 25°C for assignment of fluorine regiochemistry.

UV-vis: UV-visible spectroscopy were recored using wither a Beckman Coulter DU 800 series or Perkin Elmer Lambda 750 spectrophotometer at room temperature unless otherwise noted. All solution UV-vis experiments were run in CHCl3. Films were prepared by spin-coating $CHCl_3$ or chlorobenzene solutions onto glass

substrates. Films were annealed directly on a hot plate for 2 minutes.

Mass Spectroscopy: Full scan, low resolution FD mass spectroscopy was carried out at the department of chemsitry spectroscopy facility, University of Californa, Santa Barbara.

Electrochemistry: All electrochemical measurements were performed using CHI instrument model 730B in a standard three-electrode, one compartment configuration equipped with Ag/AgCl electrode, Pt wire and Glassy carbon electrode (dia. 3 mm), as the pseudo reference, counter electrode and working electrode respectively. Glassy carbon electrodes were polished with alumina. The cyclic voltammetry (CV) experiments were performed in anhydrous dichloromethane solution with ~0.1 M tetrabutylammonium hexafluorophosphate ($TBAPF_6$) as the supporting electrolyte at scan rate 50 mV/s unless otherwise stated. All electrochemical solutions were purged with dry Ar for 15 minutes to deoxygenate the system. Solution CV measurements were carried out with a small molecule concentration of ~1mg/mL in CH_2Cl_2. Ferrocene was used as an internal standard. The HOMO and LUMO levels were obtained by correlating the onsets ($E_{ox}^{Fc/Fc+}$, $E_{red}^{Fc/Fc+}$) to the normal hydrogen electrode (NHE), assuming HOMO of Fc/Fc^+ to be 4.88 eV.

Synthesis:

5-Fluorobenzo[*c*][1,2,5]thiadiazole (2)

In a three-neck round-bottom flask, 4-fluoro-1,2-benzenediamine (**1**) (5.5 g, 43.6 mmol) was fully dissolved in chloroform (500 mL) and triethylamine (30 mL). Thionyl chloride (7 mL, 96.0 mmol) was added drop wise via syringe. The solution stirred at 80 °C overnight. The reaction was allowed to cool and 250 mL of deionized water was added. The reaction was transferred to a separatory funnel and was several times with water. The organic phase was collected and dried over magnesium sulfate. The solution was filtered, concentrated and used directly. Recovered yield: 4.75 g (70 %). ^{1}H NMR ($CDCl_3$): δ 6.55 (dd, 1H, J = 8.4, 5.4 Hz, C*H*), 6.36 (dd, 1H, J = 10.2, 3.0 Hz, C*H*), 6.31 (td, 1H, J = 8.4, 3.0 Hz, C*H*).

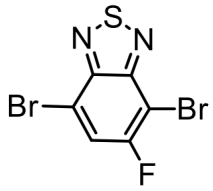

4,7-Dibromo-5-fluorobenzo[*c*][1,2,5]thiadiazole (3)

A round-bottom flask was charged with **2** (2.23 g, 14.5 mmol) followed by 48 % hydrobromic acid (30 mL). Molecular bromine (7.47 mL, 145 mmol) was added

drop wise and the reaction refluxed for 48 h. The reaction was allowed to cool to room temperature and diluted with chloroform and deionized water. The bi-phasic mixture was transferred to a separatory funnel and washed several times with water, rinsed with saturated sodium sulfite and rinsed with saturated sodium bicarbonate. Organics were collected and dried over magnesium sulfate. The solution was filtered and concentrated with silica. The compound was purified by flash column chromatography using a hexanes/chloroform gradient. Isolation of pure fractions afforded a white solid. Yield: 2.58g (57 %). ^{1}H NMR ($CDCl_3$): δ 7.79 (d, 1H, J = 8.4 Hz).

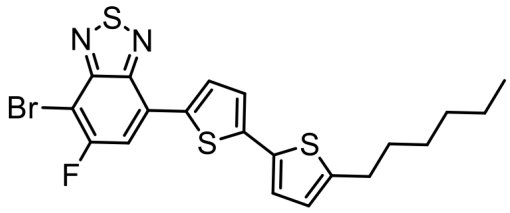

4-Bromo-5-fluoro-7-(5'-hexyl-[2,2'-bithiophene]-5-yl)benzo[*c*][1,2,5]thiadiazole (5)

Via Stille-coupling:

In a N2 filled glove box a 20 mL glass tube was charged with **3** (FBTBr2, 326 mg, 1.05 mmol), 5'-hexyl-2,2'-bithiophene-5-trimethylstannane (**4**) (432 mg, 1.05 mmol), $Pd(PPh_3)_4$ (50 mg, 0.04 mmol) and toluene (15 mL), and sealed with a Teflon® cap. The reaction mixture was heated to 80 °C for 48 h. Upon cooling, the material was then loaded onto silica and purified by flash chromatography using a

hexanes/chloroform gradient. After fraction collection and solvent removal an orange solid was obtained. Recovered yield: 294 mg (64 %). ^{1}H NMR ($CDCl_3$): δ 8.04 (d, J = 3.6 Hz, 1H, C*H*), 7.67 (d, J = 10.2 Hz, 1H, C*H*), 7.19 (d, J = 3.6 Hz, 1H, C*H*), 7.12 (d, J = 3.6 Hz, 1H, C*H*), 6.73 (d, J = 3.6 Hz, 1H, C*H*), 2.82 (t, J = 7.8 Hz, 2H, CH_2), 1.70 (m, J = 7.5 Hz, 2H, CH_2), 1.40 (br m, 2H, CH_2), 1.34 (br m, 2H, CH_2), 1.32 (br m, 2H, CH_2), 0.90 (t, J = 7.2 Hz, 3H, CH_3).

Via direct-heteroarylation:

Stock solutions were prepared of palladium acetate (0.0404 M) and pivalic acid (0.05 M) in dimethyl acetamide (DMA). In a N2 filled glove box a 10 mL glass tube was charged with **3** (FBTBr2, 52 mg, 0.168 mmol), 5-hexyl-2,2'-bithiophene (42 mg, 0.168 mmol), palladium acetate (0.17 mL, 6.7 μmol), potassium carbonate (34.8 mg, 0.252 mmol), pivalic acid, (0.2 mL, 0.1 mmol) in DMA (5 mL), and sealed with a Teflon® cap. The reaction mixture was heated to 60 °C for 48 h. The reaction was allowed to cool to room temperature, diluted with chloroform and deionized water, transferred to a separatory funnel and washed several times with water. Organics were collected and dried over magnesium sulfate. The solution was filtered and concentrated with silica. The compound was loaded onto silica and purified by flash chromatography using a hexanes/chloroform gradient. After fraction collection and solvent removal an orange solid was obtained. Recovered yield: 65.7 mg (79 %).

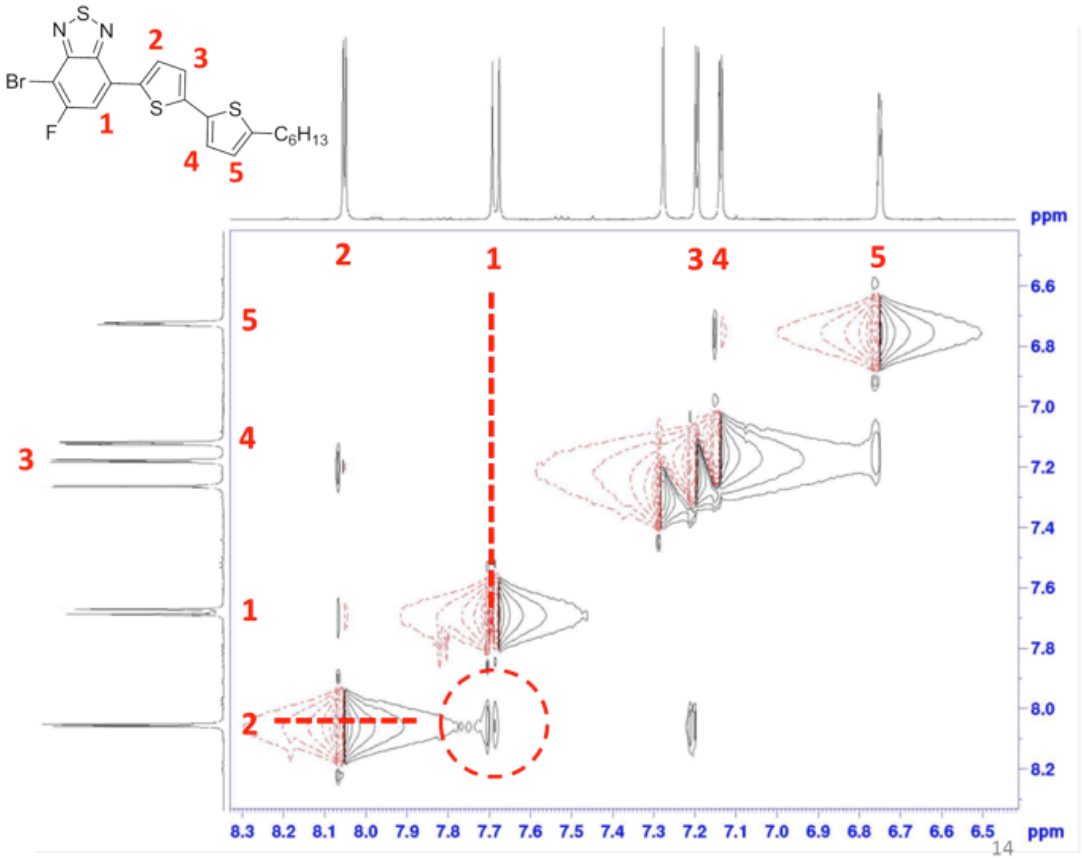

Figure 2-13. ^{1}H-^{1}H 2D NOE NMR spectrum of compound 5 in chloroform expanded to show aromatic region. Cross peak for protons 1 and 2 confirm regiochemistry of fluorine atom.

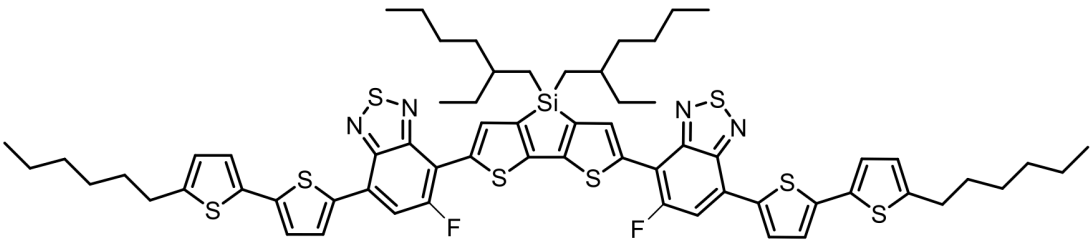

7,7'-(4,4-Bis(2-ethylhexyl)-4H-silolo[3,2-b:4,5-b']dithiophene-2,6-diyl)bis(6-fluoro-4-(5'-hexyl-[2,2'-bithiophen]-5-yl)benzo[c][1,2,5]thiadiazole) (p-

DTS(FBTTh$_2$)$_2$)

Via Stille-coupling:

In a N_2 filled glove box a 20 mL glass tube was charged with **5** (325 mg, 0.675 mmol), 5,5'-*bis*(trimethylstannyl)-3,3'-di-2-ethylhexylsilylene-2,2'-bithiophene (**6**) (250 mg, 0.338 mmol), $Pd(PPh_3)_4$ (30 mg, 0.024 mmol) and toluene (15 mL), and sealed with a Teflon® cap. The reaction mixture was heated to 100 °C for 1 minute, 125 °C for 1 minute, 140 °C for 10 minutes, 150 °C for 10 minutes, and 160 °C for 10 minutes using a Biotage microwave reactor. Upon cooling, the material was then loaded onto silica, washed with methanol and purified by flash chromatography using a hexanes/chloroform gradient *in duplicate*. After fraction collection and solvent removal a metallic purple solid was obtained. The solid was slurried in a 3:1 mixture of methanol and hexanes, sonicated for 1 hour and stirred overnight. The suspension was filtered, washed with acetone and dried in vacuo. The product was recovered as a metallic purple solid. Recovered yield: 230 mg (56 %). ^{1}H NMR ($CDCl_3$): δ 8.35 (t, 2H, C*H*), 8.05 (d, J = 3.6 Hz, 2H, C*H*), 7.75 (d, J = 6.9 Hz, 2H, C*H*), 7.20 (d, J = 3.6 Hz, 2H, C*H*), 7.13 (d, J = 3.6 Hz, 2H, C*H*), 6.74 (d, J = 3.6 Hz, 2H, C*H*), 2.83 (t, J = 7.5 Hz, 4H, CH_2), 1.71 (m, 4H, CH_2), 1.56 (br m, 2H, CH_2), 1.40 (br m, 4H, CH_2), 1.33 (br m, 16H, CH_2) 1.24 (br m, 8H, CH_2), 1.14 (br m, 4H, CH_2), 0.91 (m, 6H, CH_3), 0.84 (br m, 12H, CH_3).

Via direct-heteroarylation:

Stock solutions were prepared of palladium acetate (0.0404 M) and pivalic acid (0.05 M), and 3,3'-di-2-ethylhexylsilylene-2,2'-bithiophene (0.5 M) in dimethyl acetamide (DMA). In a N_2 filled glove box a 10 mL glass tube was charged with **5** (82 mg, 0.17 mmol), 3,3'-di-2-ethylhexylsilylene-2,2'-bithiophene (0.16 mL, 0.081 mmol), palladium acetate (0.17 mL, 6.7 μmol), potassium carbonate (35.2 mg, 0.255 mmol), pivalic acid, (0.2 mL, 0.1 mmol) in DMA (5 mL), and sealed with a Teflon® cap. The reaction mixture was heated to 60 °C for 48 h. The reaction was allowed to cool to room temperature, diluted with chloroform and deionized water, transferred to a separatory funnel and washed several times with water. Organics were collected and dried over magnesium sulfate. The solution was filtered and concentrated with silica. The compound was loaded onto silica and purified by flash chromatography using a hexanes/chloroform gradient. After fraction collection and solvent removal a metallic purple solid was obtained. Recovered yield: 36 mg (35 %).

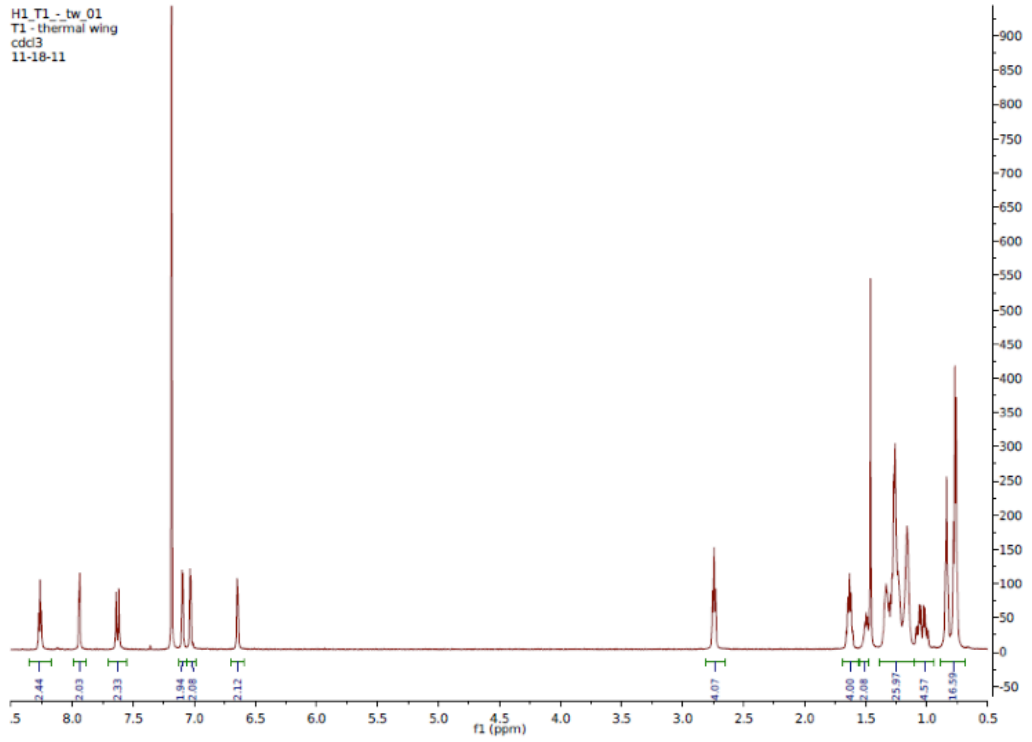

Figure 2-14. ^{1}H NMR Spectrum of molecule **2-2** in chloroform.

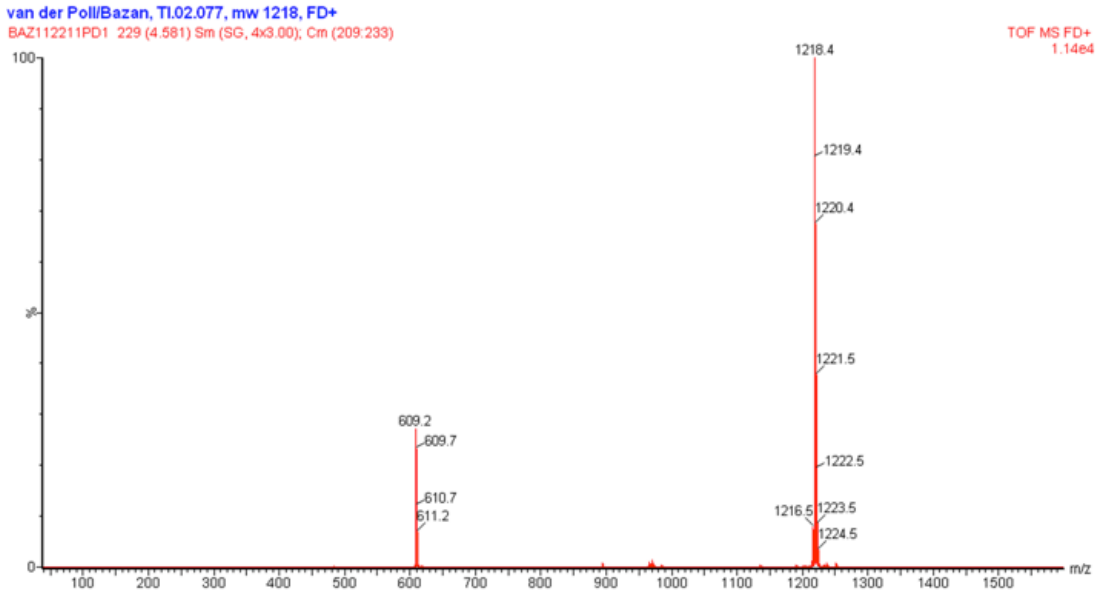

Figure 2-15. Mass spectrum of **2-2** shows M/Z peak as well as doubly charged species.

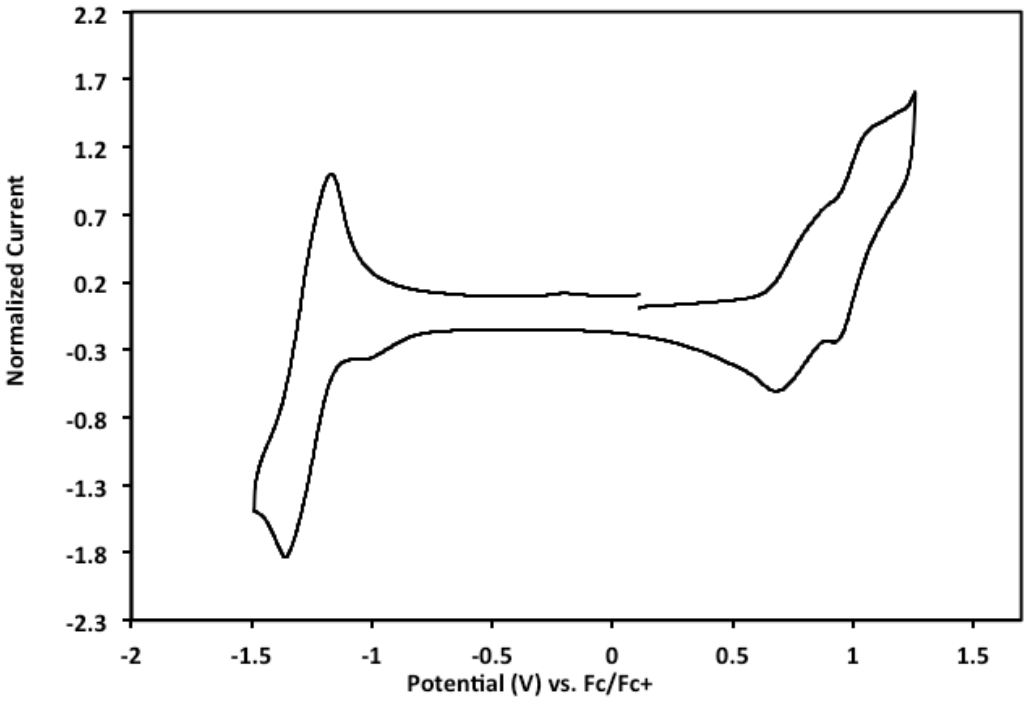

Figure 2-16. Solution cyclic voltammetry plot of **2-2** in CH_2Cl_2.

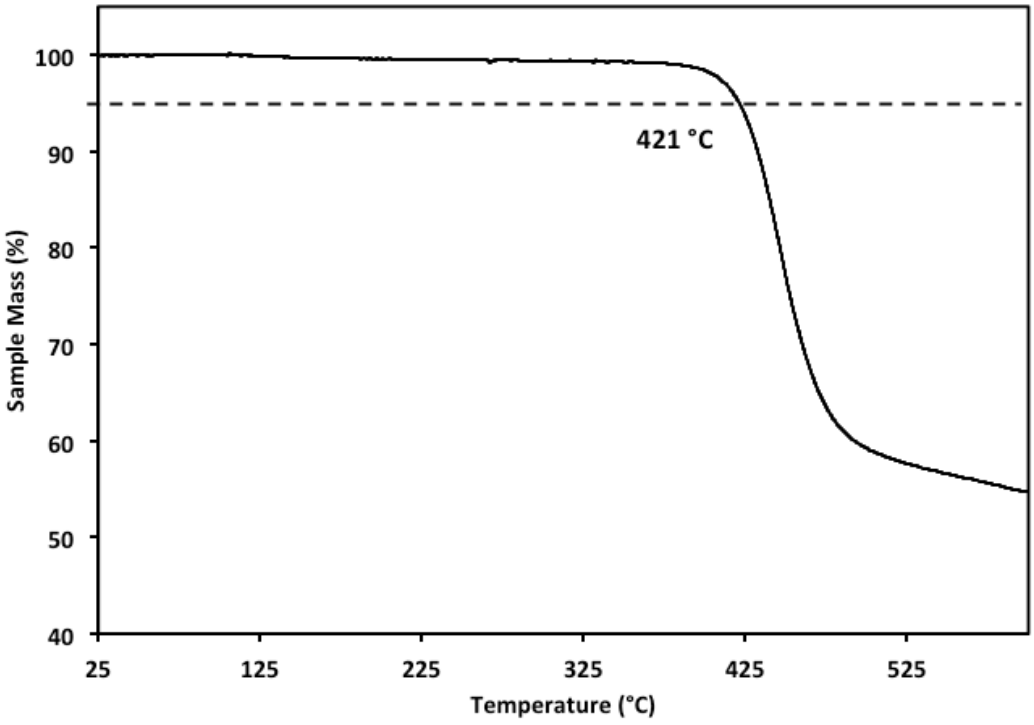

Figure 2-17. Thermogravimetric analysis plot of **2-2**. Dotted line marks 5 % mass loss, and interpreted as decomposition temperature.

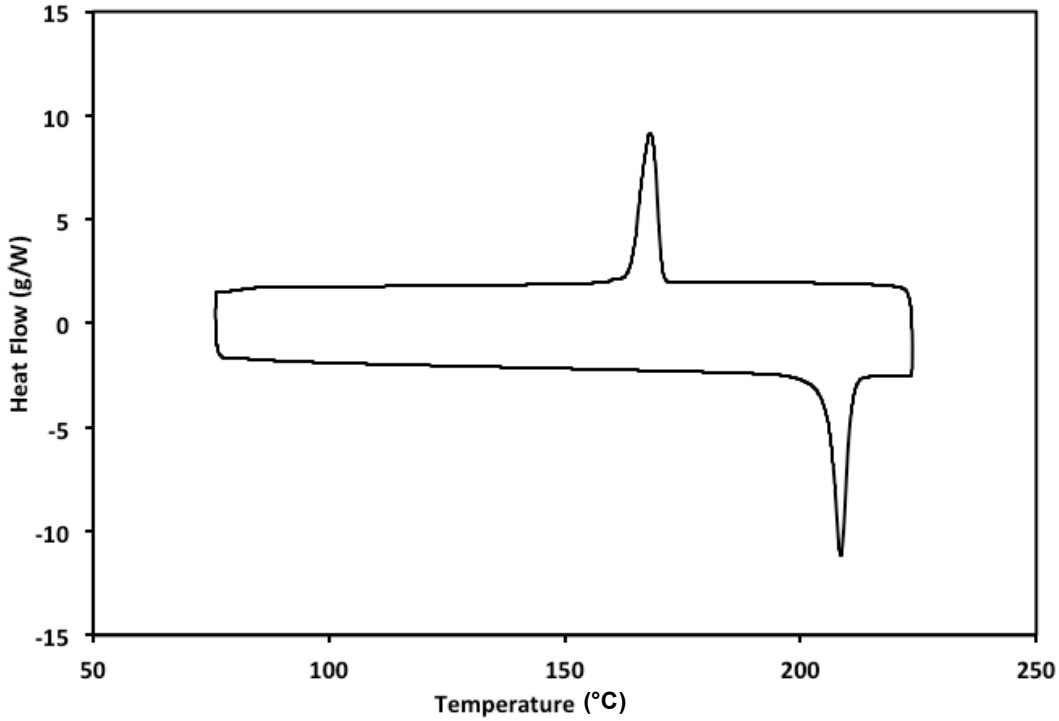

Figure 2-18. Differential scanning calorimetry plot for **2-2**.

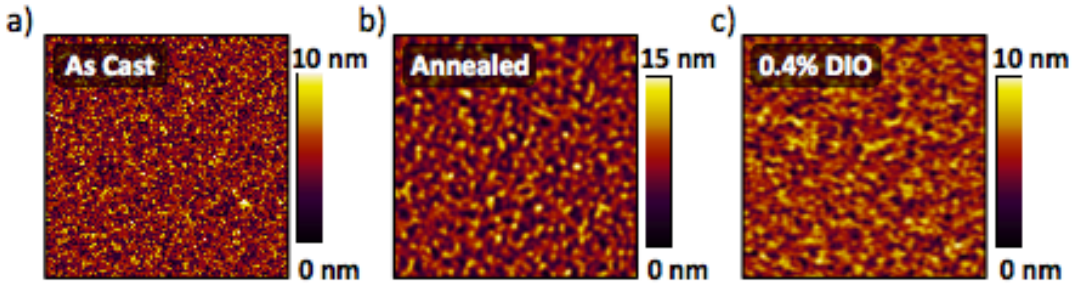

Figure 2-19. AFM topography images (10 μm × 10 μm) of films as-cast from pure chlorobenzene (a), annealed at 130 °C (b), and cast from a solution containing 0.4 % diiodooctane (c).

G. References

(1) Walker, B.; Kim, C.; Nguyen, T.-Q. *Chemistry of Materials* **2010**, *23*, 470.

(2) Li, Y.; Guo, Q.; Li, Z.; Pei, J.; Tian, W. *Energy & Environmental Science* **2010**, *3*, 1427.

(3) Roncali, J. *Accounts of Chemical Research* **2009**, *42*, 1719.

(4) Riede, M.; Mueller, T.; Tress, W.; Schueppel, R.; Leo, K. *Nanotechnology* **2008**, *19*, 424001.

(5) Tong, M.; Cho, S.; Rogers, J. T.; Schmidt, K.; Hsu, B. B. Y.; Moses, D.; Coffin, R. C.; Kramer, E. J.; Bazan, G. C.; Heeger, A. J. *Advanced Functional Materials* **2010**, *20*, 3959.

(6) Coffin, R. C.; Peet, J.; Rogers, J.; Bazan, G. C. *Nat Chem* **2009**, *1*, 657.

(7) Sun, Y.; Welch, G. C.; Leong, W. L.; Takacs, C. J.; Bazan, G. C.; Heeger, A. J. *Nat Mater* **2012**, *11*, 44.

(8) Blouin, N.; Michaud, A.; Gendron, D.; Wakim, S.; Blair, E.; Neagu-Plesu, R.; Belletête, M.; Durocher, G.; Tao, Y.; Leclerc, M. *Journal of the American Chemical Society* **2007**, *130*, 732.

(9) Henson, Z. B.; Welch, G. C.; van der Poll, T.; Bazan, G. C. *Journal of the American Chemical Society* **2012**, *134*, 3766.

(10) Handy, S. T.; Wilson, T.; Muth, A. *J Org Chem* **2007**, *72*, 8496.

(11) Schroter, S.; Stock, C.; Bach, T. *Tetrahedron* **2005**, *61*, 2245.

(12) Ernst, A.; Gobbi, L.; Vasella, A. *Tetrahedron Letters* **1996**, *37*, 7959.

(13) Tilley, J. W.; Zawoiski, S. *J Org Chem* **1988**, *53*, 386.

(14) Ratcliff, E. L.; Bakus Ii, R. C.; Welch, G. C.; van der Poll, T. S.; Garcia, A.; Cowan, S. R.; MacLeod, B. A.; Ginley, D. S.; Bazan, G. C.; Olson, D. C. *Journal of Materials Chemistry C* **2013**, *1*, 6223.

(15) Garcia, A.; Welch, G. C.; Ratcliff, E. L.; Ginley, D. S.; Bazan, G. C.; Olson, D. C. *Advanced materials* **2012**, *24*, 5368.

(16) Zalar, P.; Henson, Z. B.; Welch, G. C.; Bazan, G. C.; Nguyen, T.-Q. *Angewandte Chemie International Edition* **2012**, *51*, 7495.

(17) Welch, G. C.; Bazan, G. C. *Journal of the American Chemical Society* **2011**, *133*, 4632.

(18) Zhang, Y.; Chien, S.-C.; Chen, K.-S.; Yip, H.-L.; Sun, Y.; Davies, J. A.; Chen, F.-C.; Jen, A. K. Y. *Chemical Communications* **2011**, *47*, 11026.

(19) Peng, Q.; Liu, X.; Su, D.; Fu, G.; Xu, J.; Dai, L. *Advanced materials* **2011**, *23*, 4554.

(20) Schroeder, B. C.; Huang, Z.; Ashraf, R. S.; Smith, J.; D'Angelo, P.; Watkins, S. E.; Anthopoulos, T. D.; Durrant, J. R.; McCulloch, I. *Advanced Functional Materials* **2012**, *22*, 1663.

(21) Son, H. J.; Wang, W.; Xu, T.; Liang, Y.; Wu, Y.; Li, G.; Yu, L. *Journal of the American Chemical Society* **2011**, *133*, 1885.

(22) Chen, H.-Y.; Hou, J.; Zhang, S.; Liang, Y.; Yang, G.; Yang, Y.; Yu, L.; Wu, Y.; Li, G. *Nat Photon* **2009**, *3*, 649.

(23) Sharif, M.; Zeeshan, M.; Reimann, S.; Villinger, A.; Langer, P. *Tetrahedron Letters* **2010**, *51*, 2810.

(24) Leong, W. L.; Welch, G. C.; Kaake, L. G.; Takacs, C. J.; Sun, Y.; Bazan, G. C.; Heeger, A. J. *Chemical Science* **2012**, *3*, 2103.

(25) He, C.-Y.; Wu, C.-Z.; Qing, F.-L.; Zhang, X. *The Journal of Organic Chemistry* **2014**, *79*, 1712.

(26) Zhang, J.; Chen, W.; Rojas, A. J.; Jucov, E. V.; Timofeeva, T. V.; Parker, T. C.; Barlow, S.; Marder, S. R. *Journal of the American Chemical Society* **2013**, *135*, 16376.

(27) Wang, S.-H.; Liu, W.-J.; Zhan, H.-Y.; Zhang, H.; Liang, Y.; Tian, Y. *RSC Advances* **2013**, *3*, 23972.

(28) Poduval, M. K.; Burrezo, P. M.; Casado, J.; López Navarrete, J. T.; Ortiz, R. P.; Kim, T.-H. *Macromolecules* **2013**, *46*, 9220.

(29) Nadres, E. T.; Santos, G. I. F.; Shabashov, D.; Daugulis, O. *The Journal of Organic Chemistry* **2013**, *78*, 9689.

(30) Liu, X.-W.; Shi, J.-L.; Yan, J.-X.; Wei, J.-B.; Peng, K.; Dai, L.; Li, C.-G.; Wang, B.-Q.; Shi, Z.-J. *Organic Letters* **2013**, *15*, 5774.

(31) Guillaumet, G.; Grosse, S.; Pillard, C.; Bernard, P. *Synlett* **2013**, *24*, 2095.

(32) Kuhl, N.; Hopkinson, M. N.; Glorius, F. *Angew Chem Int Edit* **2012**, *51*, 8230.

(33) Liu, C.; Zhang, H.; Shi, W.; Lei, A. W. *Chem Rev* **2011**, *111*, 1780.

(34) Kowalski, S.; Allard, S.; Scherf, U. *ACS Macro Letters* **2012**, *1*, 465.

(35) Gierschner, J.; Ehni, M.; Egelhaaf, H.-J.; Milián Medina, B.; Beljonne, D.; Benmansour, H.; Bazan, G. C. *The Journal of Chemical Physics* **2005**, *123*.

(36) Ostroverkhova, O.; Shcherbyna, S.; Cooke, D. G.; Egerton, R. F.; Hegmann, F. A.; Tykwinski, R. R.; Parkin, S. R.; Anthony, J. E. *Journal of Applied Physics* **2005**, *98*.

(37) Johansson, T.; Mammo, W.; Svensson, M.; Andersson, M. R.; Inganas, O. *Journal of Materials Chemistry* **2003**, *13*, 1316.

(38) Rand, B. P.; Burk, D. P.; Forrest, S. R. *Physical Review B* **2007**, *75*, 115327.

(39) Scharber, M. C.; Mühlbacher, D.; Koppe, M.; Denk, P.; Waldauf, C.; Heeger, A. J.; Brabec, C. J. *Advanced materials* **2006**, *18*, 789.

(40) Marsh, R. A.; Hodgkiss, J. M.; Albert-Seifried, S.; Friend, R. H. *Nano Letters* **2010**, *10*, 923.

(41) Kim, K.; Liu, J.; Namboothiry, M. A. G.; Carroll, D. L. *Applied Physics Letters* **2007**, *90*.

(42) Zhang, Y.; Dang, X.-D.; Kim, C.; Nguyen, T.-Q. *Advanced Energy Materials* **2011**, *1*, 610.

(43) Perez, L. A.; Chou, K. W.; Love, J. A.; van der Poll, T. S.; Smilgies, D. M.; Nguyen, T. Q.; Kramer, E. J.; Amassian, A.; Bazan, G. C. *Advanced materials* **2013**, *25*, 6380.

(44) Love, J. A.; Proctor, C. M.; Liu, J.; Takacs, C. J.; Sharenko, A.; van der Poll, T. S.; Heeger, A. J.; Bazan, G. C.; Nguyen, T.-Q. *Advanced Functional Materials* **2013**, *23*, 5019.

III. Theoretical Study of Crystalline Organic Semiconductors for Solution-Processed Organic Electronics

Using ab initio calculations and classical molecular dynamics simulations coupled with complementary experimental characterization, **1-1**, **2-1**, **2-2**, and introducing **3-1**, were investigated in vacuum, solution, and in crystalline form. Independently the molecules can be described as isostructural, yet in crystalline form, two distinct crystal systems are observed with characteristic molecular geometries. The minor structural variations provide a platform to investigate the subtlety of simple substitutions, with particular focus on polymorphism and the impact of rotational isomerism. Resolved crystal structures offer an exact description of inter-molecular ordering in the solid state, enabling calculation of molecular binding energy in the crystal, as well as substituting one molecule into another's crystallographic configuration and comparing the binding energy.

A. Introduction

The vast improvements in organic photovoltaics (OPV) in the last half-decade are largely due to novel design of organic chromophores and careful optimization of device preparation.[1-4] Molecular design strategies for organic semiconducting chromophores revolve around established structure-property relationships,[5-10] where optical, electronic and physical properties can be tailored with rational selection of conjugated building blocks and peripheral side groups. This process benefits greatly from the modular nature of the building blocks used to construct such molecules,

which enables facile synthetic entry to molecular families. To that end, literature reports of new materials often include sets of structures in an attempt to extract design rules towards predictably engineering material properties. Unfortunately, the current design toolbox is limited to insight on the molecular scale, more precisely on the scale of the conjugated backbone. As described in the previous chapters, we can optimize band-gap and V_{OC} by tuning the HOMO and LUMO energies.[11] The relative distance between frontier molecular orbitals participating in charge transport intrinsically limits the V_{OC}. In tuning the band-gap one can maximize the absorption of useful solar radiation in order to generate the charge carriers responsible for current; however, it is challenging to assign a fundamental limit to J_{SC}. For a single molecular donor this factor varies in a broad range depending on the details of material preparation and device fabrication conditions, whereas the V_{OC} is usually insensitive to this. Small changes in chemical structure may drive large changes in bulk properties; many bulk properties rely on interactions between molecules, and those interactions are highly sensitive to the spatial relationships between molecules in the solid state. The aforementioned sensitivity is linked to how molecules self-assemble upon transitioning from solution to the solid state. In this chapter we analyze four molecules using experimentally determined crystal structures and theoretical methods to elucidate key factors responsible for the high sensitivity of relevant macroscopic properties, such as charge transport and photogeneration of charge carriers, to small changes in chemical structure. From a practical perspective such knowledge has the potential to deliver a predictive basis for the design of

organic semiconductors. There remains a need to better understand the impact of molecular features on the meso- and bulk scale, particularly in this context as molecular self-assembly plays a critical role in the operation of semiconducting devices.[12-15]

When establishing design rules for new materials, adhering to a consistent molecular topology grants freedom to study features that manifest as a consequence material preparation rather than by design. The results presented herein point to commonly neglected considerations, namely, that covalently linked aromatic units in organic semiconductors have two possible planar configurations, implying a vast array of potential arrangements of atoms with unknown ramifications for physical or electronic properties, and perhaps more importantly, how molecules can self-assemble upon condensation. From this perspective, small molecules present three key advantages over polymeric systems: 1) modifications can be made to structures without obfuscating structure-property relationships due to changes in the magnitude or variation in molecular weight, 2) single crystal X-ray diffraction patterns provide a precise description of the three-dimensional arrangement of molecules in the solid state and 3) full molecular structures can be included in theoretical calculations, which have proven useful in assessing molecular energy landscapes.[16-19] These advantages are especially attractive because while it may not be necessary to model a full polymer to elucidate electronic structure or how it will interact with light, their vast, diverse topology precludes a feasible investigation of even a single polymer chain. Furthermore, a resolved crystal structure offers a platform to computationally

investigate intermolecular physical and electronic relationships.[20] It is important to acknowledge that single crystals are not representative of the entire bulk, but provide insight into what is likely a preferential arrangement of molecules and structural moieties upon transition from solution to the solid state. It is challenging to effectively use theory to predict macroscopic physical and electronic properties because spun-cast organic semiconductors largely comprise amorphous domains, but the nature of resultant crystalline species gives clues to what is happening in the casting solution.

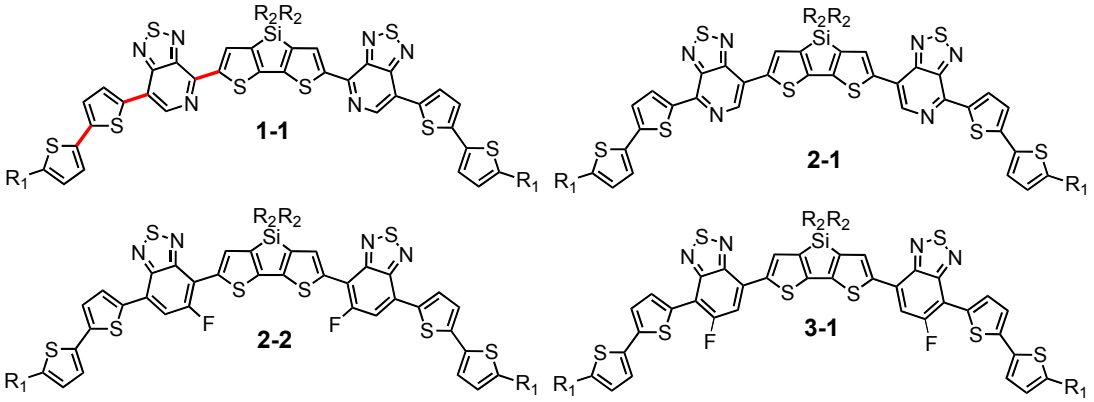

Figure 3-1. Chemical structures of **1-1**, **2-1**, **2-2**, and **3-1**. R_1 = C_6H_{13}, R_2 = 2-ethylhexyl. Bold red bonds indicate location of dihedrals 1-3, from left to right, respectively

The four molecules **1-1**, **2-1**, **2-2**, and introducing **3-1**, shown in Figure 3-1, represent a class of molecules that have demonstrated promising performance in solution processed bulk-heterojunction solar cells owing to their useful physical, optical, and electronic properties (REFx). In this molecular family, consistencies are observed across crystal lattice arrangements for different molecules. Single crystals

were grown via solvent vapor diffusion of molecules **1-1**, **2-2** and **3-1**, and attempted unsuccessfully for molecule **2-1**. The geometry of the conjugated backbone (CBB) shown in Figure 3- 1 is also the geometry of molecule **1-1** in its observed monoclinic crystal structure, as well as one observed polymorph of **3-1**. This class of molecules has been shown to typically crystallize in optimized geometries, yet we observe a violation of this for two crystals; molecule **2-2** and one polymorph of **3-1** exhibit linear CBBs in a triclinic unit cell. There are no obvious steric or electrostatic explanations for this discrepancy considering molecule **3-1** appears in each configuration in the experimentally determined lattices. Lattices structurally similar to crystal **1-1** will be referred to as type *a*, and lattices similar to crystal **2-2** as type *b*. The molecular features observed in experimentally determined crystals that distinguish lattice type *b* from type *a* are three flipped dihedrals in the CBB. The two implications that follow from these observations are 1) a significance of rotational isomerism, and 2) a preferential formation of lattices comprising un-optimized geometries. While molecular shape is cited as an important facet of solid-state packing, and ongoing efforts seek to control shape via connectivity and conformational locks,[21-28] neither of the aforementioned implications have been represented in molecular design strategies.

Conformational space of conjugated molecules is governed by two kinds of non-rigid dihedrals: those involving single bonds in a π-conjugated segment and also dihedrals in aliphatic side-chains. To separate these two classes we start with considering the hydrogen-substituted CBBs of the discussed molecules. Each CBB

has a total of six single bonds that link aromatic units, indicating two possible planar configurations. It is important to point out that while these bonds can be assigned an orientation, they do not necessarily adopt exactly 0 or 180 degree dihedral angles due to sterics. The conformational space of each CBB consists of 2^6=64 rotational isomers, or rotamers. Most of the electronic properties of an isolated molecule, such as ionization potential (IP), electron affinity (EA) and excitations, are determined almost exclusively by the conjugated backbone. In other words, a hydrogen-substituted CBB gives an accurate representation of the whole molecule (as accurate as current state-of-the-art DFT is). Second, molecules used in photovoltaic devices typically consist of tens to hundreds of atoms, including side chains. This results in a huge conformational space countable only by special techniques like replica exchange.[29] For intra-molecular electronic properties (molecules in solution) this variety of conformations results only in some broadening of observables such as IP/EA or excitation energies. Typically this broadening is smaller than the vibrational broadening.[20] In contrast, intermolecular properties such as electronic couplings or structural arrangements are highly sensitive to variations in structure of individual molecules. In this section we discuss electronic and structural properties of isolated molecules in vacuum and solution.

B. Conformational Isomerism

Before comparing energies of rotamers we need to understand how to compare them. First of all, potential energy surfaces for the dihedrals of interest are sensitive

to computational method (experimental and supplementary information section). Despite the fact that our default ab initio method was chosen to make valid comparisons with the available experimental data (CAM-B3LYP density functional, 6-31g* basis set), the uncertainty of calculated differences in energies is larger than 10 meV. Additionally, the difference in thermal vibrational energies between the most important rotamers does not exceed 10 meV. The trend is systematic: the higher a local minimum, the lower its zero-point vibrational energy; however this effect is not specific for a particular class of molecules and is spread over the entire vibrational spectrum. Therefore we will neglect this contribution to energy. Finally, because we have a heteroatomic conjugated system, we have large atomic charges (experimental and supplementary information), and thus rotamer energetics is sensitive to solvent and side-chains.

Table 3-1. Energy cost (in meV) for planarizing conformation "a" (E_p), flipping dihedrals (E_{fn}), and the corresponding rotational barriers (E_{bn}) for conjugated backbone in vacuum and chloroform. Dihedrals 4,5,6 are symmetric to 3,2,1, respectively. All geometries are relaxed.

mol.	Env.[a]	E_p[b]	E_{f1}[c]	E_{f2}	E_{f3}	E_{b1}[d]	E_{b2}	E_{b3}
1-1	vac.	9	31	34	66	118	187	407
2-1	vac.	6	32	65	28	134	405	182
2-2	vac.	9	31	30	24	119	204	209
3-1	vac.	9	31	26	22	121	200	210
1-1	$CHCl_3$	8	27	13	65	123	159	361
2-1	$CHCl_3$	4	27	64	7	136	358	153

2-2	$CHCl_3$	8	27	6	17	125	173	171
3-1	$CHCl_3$	8	27	19	0	124	174	168

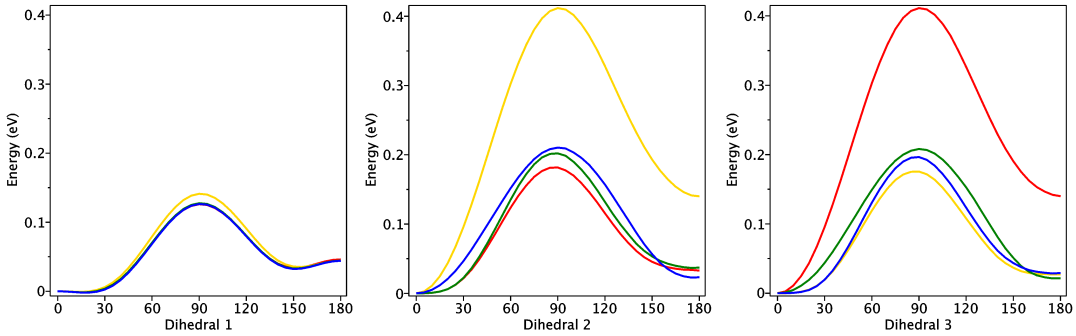

Figure 3-2. Example PES scans for dihedrals for the planarized conjugated backbone in vacuum (unrelaxed geometry) of **1-1** (red), **2-1** (yellow), **2-2** (green) and **3-1** (blue).

Initial efforts targeted dihedral angles within each conjugated backbone. Table 3-1 and Figure 3-2 provide a concise summary of the energetic landscape that describes the dihedrals within the CBB of each molecule using three values: planarization energy (E_p), the energy cost of flipping a dihedral from the optimized configuration (E_{fn}, where "n" is the bond defining the axis of rotation), and the energy barrier for dihedral rotation (E_{bn}). For all four isolated molecules the geometry of the conjugated backbone (CBB) at the energetic global minimum is congruent to the one chosen for illustration in Chart 1. A simplification follows from the observed independence of different rotations accurate within few meV, allowing for the following representation of the rotamer energy:

Equation 3-1: $$E = E_0 + \sum_{n=1}^{6} b_n E_n,$$

where E_0 is the energy of the molecule in the optimized geometry, b_n is a binary operation equal to 0 if the corresponding dihedral is closer to zero than to 180º and 1 otherwise, and E_n is the energy cost for flipping dihedral n. Specific values for dihedral angles and energetic costs can be found in experimental and supplementary information section for all 34 unique geometries of each molecule without aliphatic side-groups. Note a dramatic reduction in most of the energies for molecules in a solvent. All the rotamers are thermally equilibrated at room temperature in nanoseconds to microseconds (picosecond vibrational period upscaled by a Boltzmann factor, confirmed by molecular dynamics). It is worth noting for the observed flipped dihedrals 1, 3 and 4, in crystal geometries of **2-2** and **3-1**, the E_{fn} energies are approximately at or below kT at 300 °K. Dihedrals 3 and 4 in **1-1** and dihedrals 2 and 5 in **2-1** are trapped in a global minimum effectively locking their conformations. In the case of **1-1**, this would preclude adopting the geometry found in the crystal of **2-2**, or type *b*. Figure 3-3 visualizes these results as a Boltzmann distribution based on the energy of all 64 possible conformations, organized from the lowest energy, most populated geometry to the highest energy, least populated. This plot highlights the fact that **2-2** and **3-1** are far less encumbered. For example, the statistical weight of the lowest energy conformation varies from 1 in 5 for an ensemble of **1-1** to 1 in 15 for an ensemble of **2-2**.

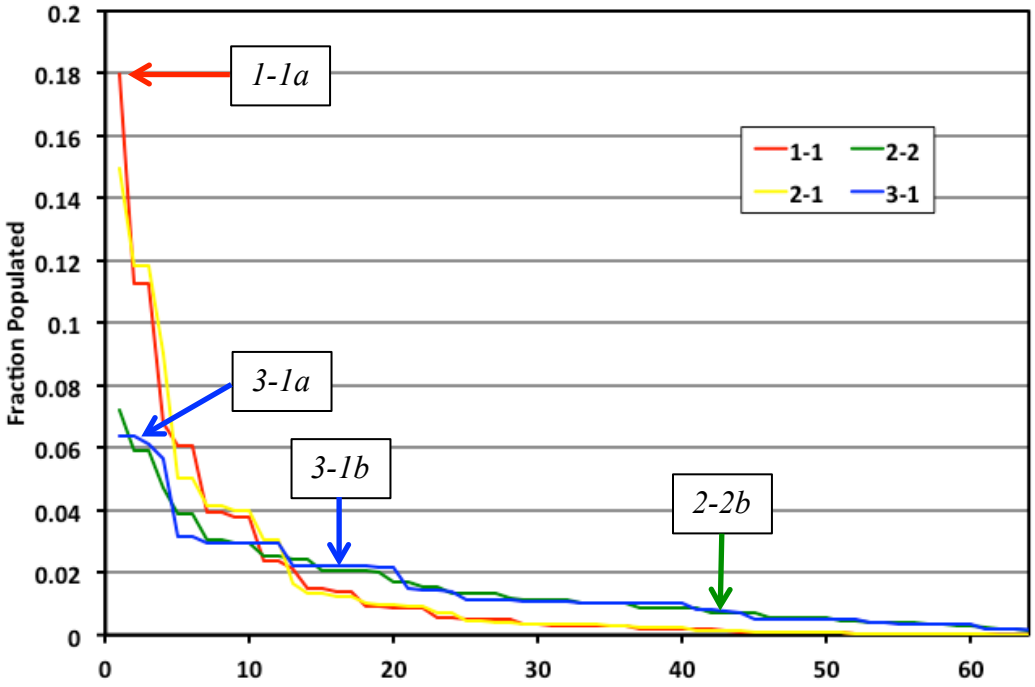

Figure 3-3. Boltzmann distribution of 64 possible rotamers ofr molecules **1-1**, **2-1**, **2-2** and **3-1**. Boxes and arrows indicate location of experimentally observed geometries in crystals.

It is important to recognize that a solution prepared for active layer deposition comprises dynamic molecular species – an inevitable aspect of solution processing. Molecular dynamics (MD) calculations were employed for a dynamic perspective and estimation of free energy. Simulations show that aliphatic side-chains appended to the silicon bridgehead demonstrate a propensity to interact with the π-system, which may be non-trivial to the self-assembly process. Additionally, an interesting distinction between molecules **1-1** and **2-2** arises with the inclusion of side-chains regarding the barrier to rotation. Due to a favorable interaction between the aliphatic

hydrogen atoms and the electronegative fluorine attached to the acceptor, side-chains stabilize rotation of dihedrals 3 and 4 from the lowest energy conformation in molecule **2-2**. In fact, by taking a statistical sampling of snapshots during MD simulations indicated that for a single conformational isomer of the conjugated backbone, the side chains can impact total energy by ± 300 meV. This serves as a reminder that while the conjugated backbone sufficiently describes electronic properties of the whole molecule, side groups have a substantial impact on the total energy and dynamic processes, even chemically inert aliphatic side-chains.

In terms of understanding how and what types of crystalline domains form during the transition from solution to the solid state, calculations for isolated molecules offer a practical approach to assessing a molecules' behavior in solution. Not all conformations that are statistically important in solution are presented in crystals, but everything that is found in the crystal is present in solution. The lesson here is intra-molecular properties constrain the conformational space, but not enough to dictate the molecular conformation in the crystal structure. Next we look to the experimentally determined lattice in order to elucidate what makes this particular arrangement preferable.

C. Crystal Structures

Table 3-2. Structural and electronic properties of simulated crystals relaxed in an MM3 force field. Note that 3-1a' and 3-1a" are two ordered crystals of the experimentally observed disordered crystal; 3-1a and 3-1a' have the same CBB.

Parenthetical values were calculated using the observed lattice rather than one relaxed using an MM3 force field. Binding energies are reported on a per-molecule basis.

entry	binding energy (eV)	*intra*-stack binding energy (eV)	*inter*-stack binding energy (eV)	stack translation vector (Å)	exciton coupling (meV)	hole coupling (meV)	conformation energy (eV)
1-1*a*	3.39	2.04	0.45	5.4 (5.2)	65 (63)	53	0
1-1*b*	3.1	1.88	0.41	8.7	69	121	0.16
2-1*a*	3.28	2.06	0.41	5.7	45	40	0
2-1*b*	3.23	1.86	0.46	9.2	51	126	0.04
2-2*a*	2.99	2.08	0.30	5.7	57	65	0
2-2*b*	3.34	2.15	0.40	8.9 (9.3)	43 (30)	127	0.06
3-1*a*	3.14	2.06	0.36	5.7	65	44	0
3-1*a*'[a]	3.16	2.07	0.36	4.5 (4.4)	10 (113)	100	0
3-1*a*''[a]	3.18	2.02	0.39	4.7 (4.4)	80 (88)	75	0.02
3-1*b*	3.31	2.03	0.43	9.4 (9.3)	56 (46)	105	0.03

Measured and calculated properties of all the studied crystals are summarized in Table 3-2. All molecules studied in the present work have a common crystal motif: a closed packed lattice of one-dimensional π-stacks. Fig. 3-4 shows portions of lattices for molecule **1-1** and **2-2** (Fig 3-4a and 3-4b, respectively). The CBB of all the molecules in a single π-stack are aligned with typical π-π stacking distance of 3.5 Å. In the direction perpendicular to the π-stacks a triangular lattice topology is well resolved, indicative of close packing. All the crystals have nearly the same molecular density while having very different microstructure, but all are consistent with the space filling being an important driving force for crystal formation. The key difference between the studied crystals is in the arrangement of molecules in a stack. From this perspective two stack types are observed: parallel and antiparallel as

determined by the mutual orientation of the neighboring molecules in a stack. An intrinsic static disorder, which is typical for crystals of such molecules, involves both side chain and CBB conformations.

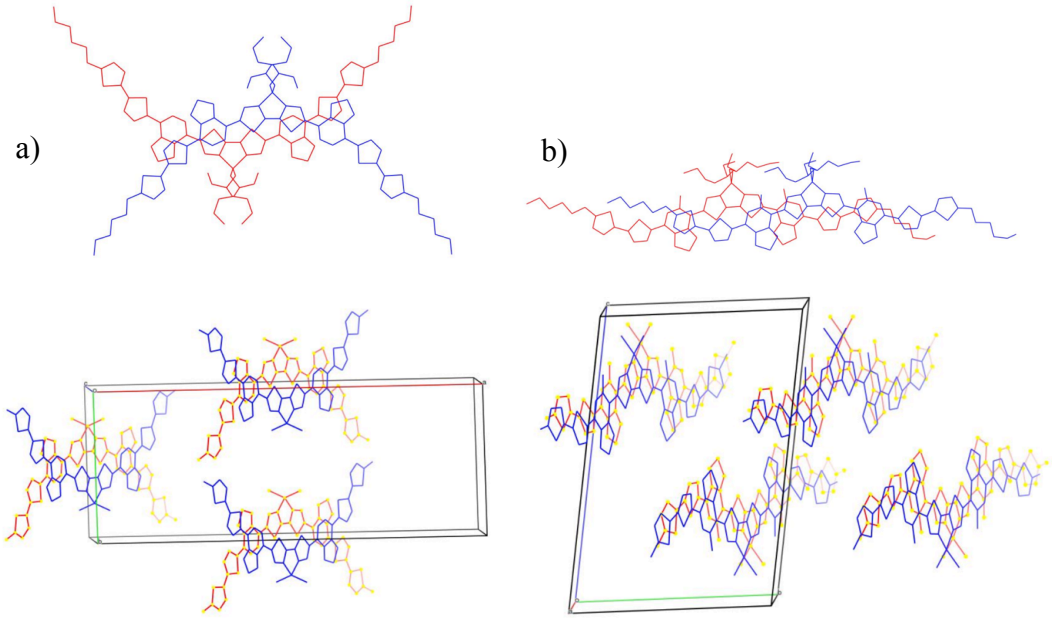

Figure 3-4. Top-down perspective of dimers and π-stacks for molecules **1-1** (a) and **2-2** (b). For clarity, molecules are shown from a perspective parallel to π-stacks, with neighboring stacks.

To understand the experimental data we performed MM3 force field calculations (see Table 3-2). Because a proper statistical sampling of such crystals is computationally prohibitive, in the calculations the static disorder is cleaned from the experimentally observed structure and then relaxed with MM3 force field. MD in a large supercell comprising two π-stacks, each four molecules tall, shows the

stability of the relaxed structure. For molecule **3-1** two conformations, 3-1a' and 3-1a", coexisting in a single crystal are considered separately. Among polymorphs not observed experimentally we consider only those corresponding to experimentally observed crystals **1-1** and **2-2** (1-1a and 2-2b in Table 3-2). By definition, molecular binding energy ($E_{lattice}$) in a crystal is calculated as follows:

$$E_{lattice} = E_{unit\ cell}/n - E_{molecule},$$

where $E_{unit\ cell}$ is the total energy per unit cell, "n" is the number of molecules in the unit cell, and $E_{molecule}$ is the energy of an isolated molecule. The same method can be applied to calculate intra-stack binding energy. We begin with comparing intra- and inter-stack binding energies. The latter is the difference between the total and intra-stack interaction energies divided by the number of interacting stack directions, which is three for the triangular lattice (See figure 3-5). We see that the intra-stack binding energy, which is about 2.0 eV/mol, is much stronger than the inter-stack binding energy, which is about 0.4 eV/mol/stack.

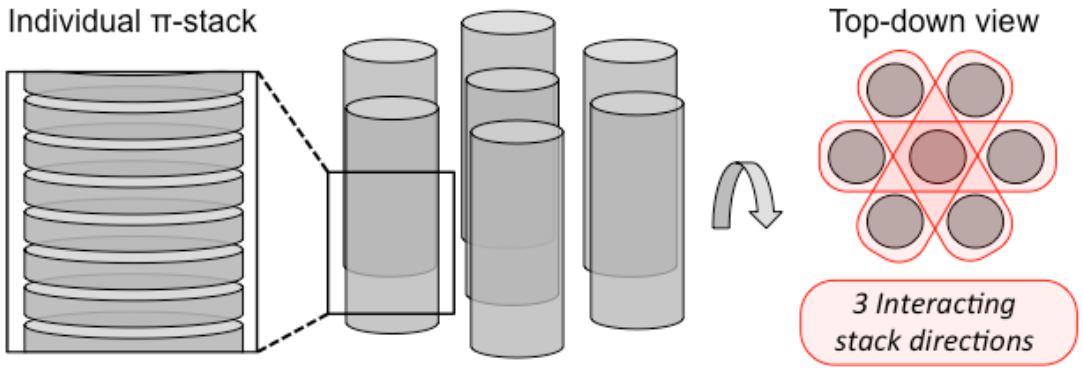

Figure 3-5. Cartoon schematic of a triangular lattice highlighting dominant interactions.

The rationalization of the observed structural trends is straightforward based on the three energies from Table 3-2: conformation energy, intra-stack and inter-stack binding energies. For molecule **1-1** all the three components give a strong preference for the crystal structure observed experimentally (1-1a). For molecule **2-2** the experimentally observed conformation 2-2b is not the lowest conformation in a solution, but the calculated energy difference, 60 meV, is small enough for this conformation to be populated at the room temperature. In addition, half of this energy is due to the rotation of the terminal thiophene, which, at a π-stack terminus would not have it's rotation impeded by a co-facial π-system (see Figure 3-4b). The intermolecular binding energies give a strong preference for the observed crystal structure (2-2b). For molecule **2-1** the conformations 2-1a and 2-1b have an even smaller energy difference in solution. The intra-stack binding energy prefers the structure 2-1a, whereas the inter-stack interactions give preference to the structure 2-1b. We postulate that the frustration between the two polymorphs prevents the formation of single crystals, and in fact we have not yet succeeded in the preparation of single crystals for this molecule. For molecule **3-1** the experimentally observed conformations are nearly isoenergetic in a solution. The intra-stack binding energies are also nearly the same for each, and there is little variation in inter-stack energies, in agreement with the observation of two polymorphs for molecule **3-1**.

Finally we discuss electronic properties of the studied crystals. Exciton and hole nearest-neighbor intermolecular couplings computed by DFT are shown in Table 3-

2. A clear trend is observed for hole-couplings: type “b” crystal structure has 2-3 times larger coupling than type “a” structure. In addition, the centroid-to-centroid distance between neighboring molecules in a π-stack, or the π-stack translation vector, is 1.6 times larger for the structural type “b”. Because a zero-field mobility along the π-stack is proportional to the squares of these two quantities the type “b” crystal structure has an order of magnitude larger hole mobility for all the studied molecules. Interestingly, for the structure “b” the side groups attached to the Si atom play an important role in fixing the observed slip-stack geometry. For example, if we remove the side groups for the structure 2-2b, the π-stack translation vector shrinks to 7.3 Å, and additional polymorph appears 60 meV/mol higher in energy with the short translation vector of 4.4 Å.

D. Conclusions

In conclusion, we have used computational methods to reconcile disparate molecular packing arrangements for isostructural molecules that arise from seemingly innocent molecular features. The calculated rotational barriers and relative energies of different rotamers corroborate that in fact a diverse distribution of molecular species is likely to exist in a sample of material that exhibits this highly common form of asymmetry. Single crystal structures indicate that an optimized molecular geometry cannot be assumed to represent a dominant species in the bulk or as the most likely candidate for single crystal formation. It follows intuitively that even subtle structural variations give rise to changes in intermolecular interactions.

The calculated binding energies in the lattice favor the observed crystal structures. This work assists in assessing key structural features of organic semiconductors more comprehensively, both retrospectively and moving forward. As this work is extended, one can envision an enhanced understanding at the mesoscopic scale and the possibility of a more ground-up approach to molecular design.

E. Experimental and Supplementary Information Computational

Methodology: Ab-initio calculations on single molecules are performed within DFT approach (TDDFT for excited states) using CAM-B3LYP density functional[30] and reasonably small 6-31g* basis set. A priori, for the studied class of molecules CAM-B3LYP fits the Koopman's theorem within 0.2 eV, see the supporting information and Ref.[31] A posteriori, this functional provides the most accurate description for the whole set of available experimental data including intramolecular geometry, IP/EA, and excitations. Importantly, though the absolute accuracy of the used DFT methods is limited, the relative changes in IP/EA and excitaion energies are well reproduced on a scale smaller than 0.1 eV.

A large subset of calculations is repeated using other density functionals and basis sets. In particular, the inclusion of polarization orbitals on hydrogens to improve the description of weak hydrogen bonds influencing the rotamer energetics has negligible 1-2 meV effect (and population of those orbitals is negligible). Total energies are compared also to those obtained within MP2 approach. Electrostatic effects of solvent or crystalline environment are accounted for by including a conductor-like polarizable continuum model (CPCM)[32] with the appropriate static

and optical dielectric constants. All the ab initio calculations are performed using the Gaussian 09 program.[33] Computations of IP/EA, polaron reorganization energy are detailed in Ref.[20]

Molecular dynamics and full crystal calculations are performed with MM3 force field[34] using TINKER program.[35] Comparison with ab initio calculations and experimental geometries shows that this force field gives qualitatively correct results except for PES for dihedrals 1 and 6 which is inaccurate in MM3 force field. Technical details can be found in the supporting information.

General Details: Preparations were carried out on a bench top or under an atmosphere of dry, O_2-free N_2 employing both Schlenk line techniques and a Vacuum Atmospheres inert atmosphere glove box. Deuterated chloroform ($CDCl_3$) was purchased from Cambridge Isotopes Laboratory and used as received. All reactants and reagents are commercially available and used as received, unless otherwise noted.

General Synthesis: Compound 5,5'-bis(trimethylstannyl)-3,3'-di-2-ethylhexylsilylene-2,2'-bithiophene ($DTS(SnMe_3)_2$) and 5'-hexyl-2,2'-bithiophene-5-trimethylstannane were prepared by methods similar to those reported in the literature.[36]

NMR Spectroscopy: ^1H and ^{13}C nuclear magnetic resonance (NMR) spectroscopy spectra were recorded on a Varian VNMRS 600 MHz Spectromenter at 25°C unless otherwise noted. ^1H and ^{13}C NMR spectra are referenced to SiMe4 using the residual

solvent peak impurity of the given solvent. Chemical shifts are reported in ppm and coupling constants in Hz as absolute values. 2D NOE ^{1}H-^{1}H correlation experiments were completed on a Bruker Avance-500 MHz spectrometer at 25°C for assignment of fluorine regiochemistry.

UV-vis: UV-visible spectroscopy were recored using a Perkin Elmer Lambda 750 spectrophotometer at room temperature unless otherwise noted. All solution UV-vis experiments were run in CHCl3. Films were prepared by spin- coating $CHCl_3$ or chlorobenzene solutions onto glass substrates. Films were annealed directly on a hot plate for 2 minutes.

Mass Spectroscopy: Full scan, low resolution FD mass spectroscopy was carried out at the department of chemsitry spectroscopy facility, University of Californa, Santa Barbara.

Electrochemistry: All electrochemical measurements were performed using CHI instrument model 730B in a standard three-electrode, one compartment configuration equipped with Ag/AgCl electrode, Pt wire and Glassy carbon electrode (dia. 3 mm), as the pseudo reference, counter electrode and working electrode respectively. Glassy carbon electrodes were polished with alumina. The cyclic voltammetry (CV) experiments were performed in anhydrous dichloromethane solution with ~0.1 M tetrabutylammonium hexafluorophosphate ($TBAPF_6$) as the supporting electrolyte at scan rate 50 mV/s unless otherwise stated. All electrochemical solutions were purged with dry Ar for 15 minutes to deoxygenate

the system. Solution CV measurements were carried out with a small molecule concentration of ~1mg/mL in CH_2Cl_2. Ferrocene was used as an internal standard. The HOMO and LUMO levels were obtained by correlating the onsets ($E_{ox}^{Fc/Fc+}$, $E_{red}^{Fc/Fc+}$) to the normal hydrogen electrode (NHE), assuming HOMO of Fc/Fc^+ to be 4.88 eV.

Synthesis:

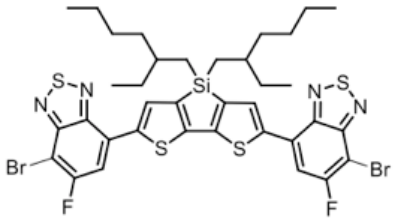

7,7'-(4,4-Bis(2-ethylhexyl)-4H-silolo[3,2-b:4,5-b']dithiophene-2,6-diyl)bis(6-fluoro-4-bromo-benzo[c][1,2,5]thiadiazole) **(DTS(FBT-Br)$_2$)**

In a N_2 filled glove box a 20 mL glass tube was charged with 4,7-Dibromo-5-fluorobenzo[*c*][1,2,5]thiadiazole (397 mg, 1.27 mmol), 5,5'-*bis*(trimethylstannyl)-3,3'-di-2-ethylhexylsilylene-2,2'-bithiophene (316 mg, 0.42 mmol), $Pd(PPh_3)_4$ (50 mg, 0.04 mmol) and toluene (15 mL), and sealed with a Teflon® cap. The reaction mixture was heated to 100 °C for 1 minute, 125 °C for 1 minute, 150 °C for 1 minute, and 165 °C for 30 minutes using a Biotage microwave reactor. Upon cooling, the material was then loaded onto silica and purified by flash chromatography using a hexanes/chloroform gradient. After fraction collection and solvent removal a purple solid was obtained. Recovered yield: 332 mg (90 %). **^{1}H NMR** ($CDCl_3$): δ 8.11 (t, 2H, C*H*), 7.65 (d, J = 10.2 Hz, 2H, C*H*), 1.43 (br m, 2H,

C*H2*), 1.25 (br m, 4H, C*H2*), 1.18 (br m, 4H, C*H2*), 1.11 (br m, 6H, C*H3*), 1.00 (br m, 4H, C*H3*), 0.73 (m, 12H, C*H3*).

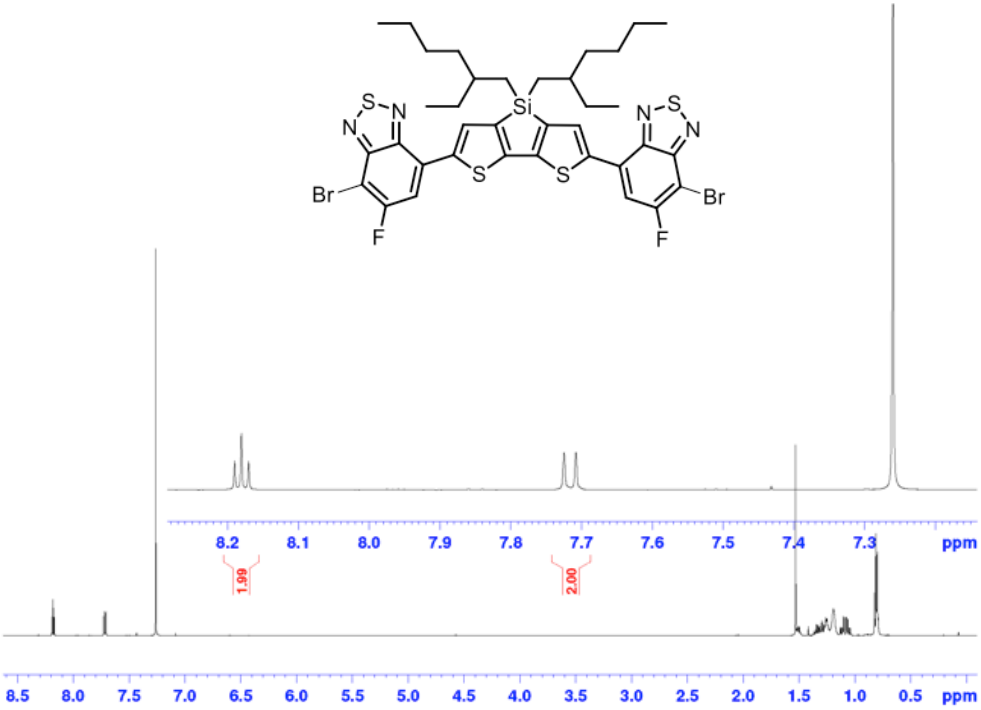

Figure 3-6. ^{1}H NMR Spectrum of molecule DTS(FBT-Br)$_2$ in chloroform.

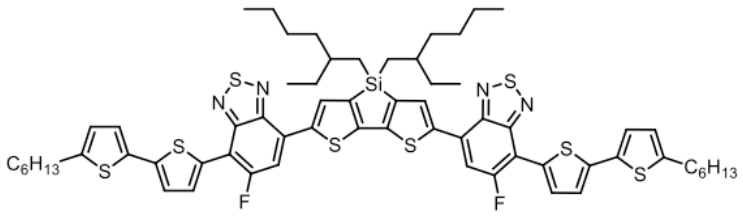

7,7′-(4,4-bis(2-ethylhexyl)-4H-silolo[3,2-b:4,5-b′]dithiophene-2,6-diyl)bis(5-fluoro-4-(5′-hexyl-[2,2′-bithiophen]-5-yl)benzo[*c*][1,2,5] thiadiazole) **(3-1)**

In a N2 filled glove box a 20 mL glass tube was charged with DTS(FBT-Br)$_2$ (100 mg, 0.11 mmol), 5'-hexyl-2,2'-bithiophene-5-trimethylstannane (94 mg, 0.23 mmol), Pd(PPh$_3$)$_4$ (30 mg, 0.024 mmol) and toluene (15 mL), and sealed with a Teflon® cap. The reaction mixture was heated to 100 °C for 1 minute, 125 °C for 1 minute, 150 °C for 1 minute, and 165 °C for 30 minutes using a Biotage microwave reactor. Upon cooling, the material was then loaded onto silica, washed with methanol and purified by flash chromatography using a hexanes/chloroform gradient *in duplicate*. After fraction collection and solvent removal a metallic purple solid was obtained. The solid was slurried in a 3:1 mixture of methanol and hexanes, sonicated for 1 hour and stirred overnight. The suspension was filtered, washed with acetone and dried in vacuo. The product was recovered as a metallic purple solid. Recovered yield: 79 mg (59 %). **^{1}H NMR** (CDCl3): δ 8.20 (t, 2H, C*H*), 8.16 (d, J = 4.2 Hz, 2H, C*H*), 7.69 (d, J = 13.2 Hz, 2H, C*H*), 7.20 (d, J = 4.2 Hz, 2H, C*H*), 7.12 (d, J = 3.0 Hz, 2H, C*H*), 6.72 (d, J = 3.6 Hz, 2H, C*H*), 2.83 (t, J = 7.8 Hz, 4H, C*H2*), 1.71 (m, 4H, C*H2*), 1.56 (br m, 2H, C*H2*), 1.40 (br m, 4H, C*H2*), 1.33 (br m, 16H, C*H2*) 1.24 (br m, 8H, C*H2*), 1.12 (br m, 4H, C*H2*), 0.90 (m, 6H, C*H3*), 0.83 (br m, 12H, C*H3*).

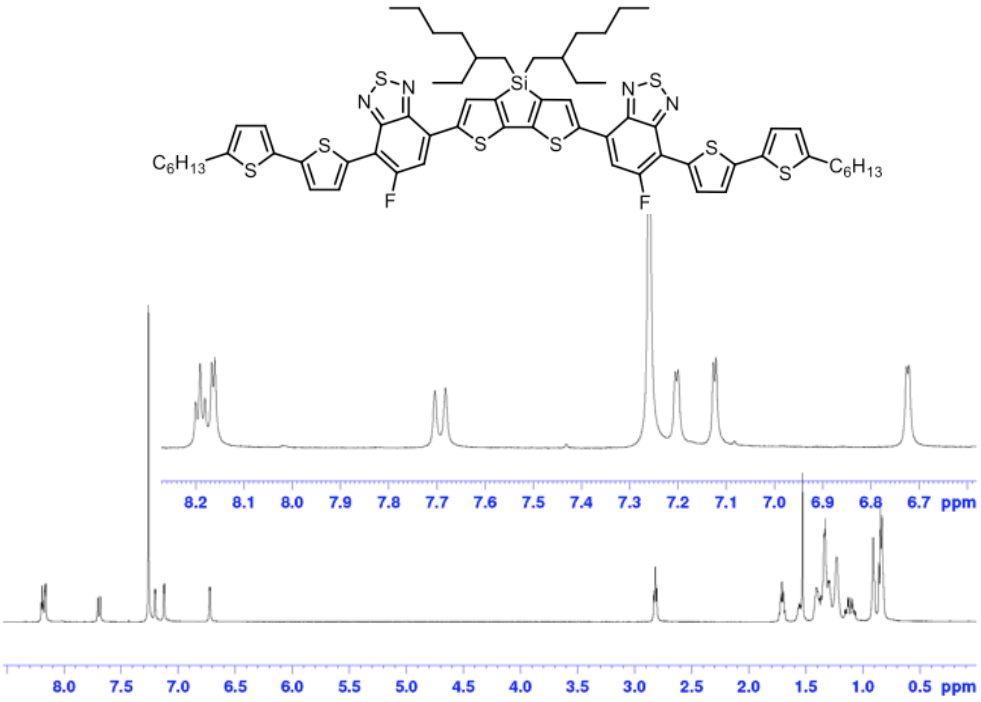

Figure 3-7. ^{1}H NMR Spectrum of molecule **3-1** in chloroform.

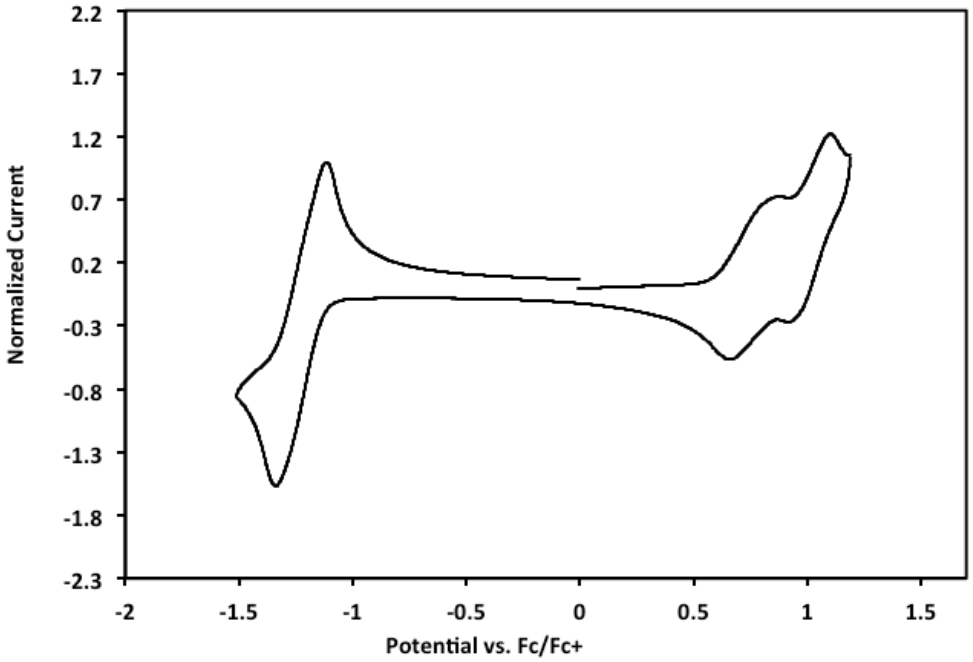

Figure 3-8. Solution cyclic voltammetry plot of **3-1** in CH_2Cl_2.

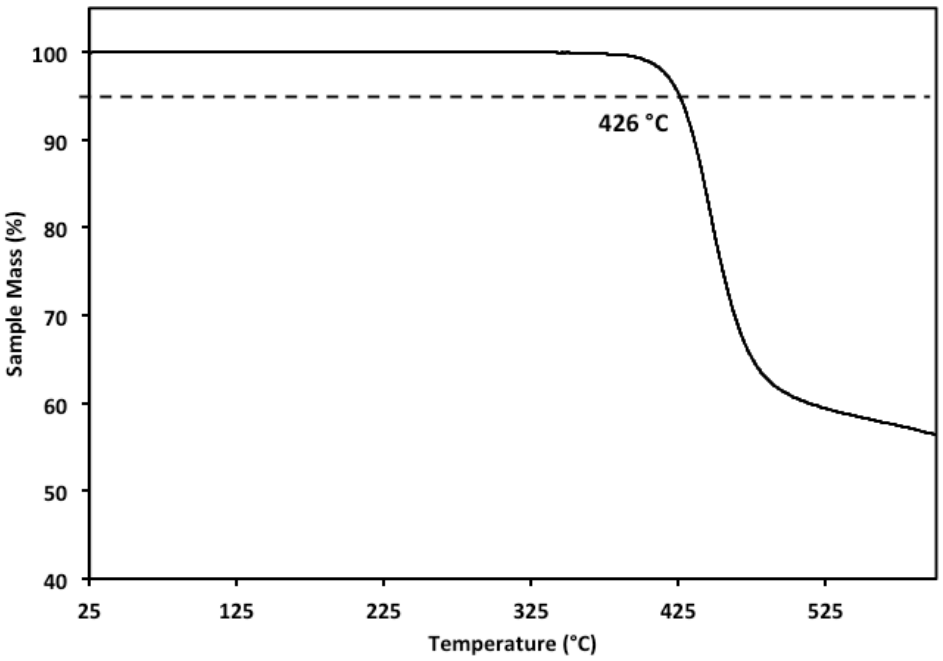

Figure 3-9. Thermogravimetric analysis plot of **3-1**. Dotted line marks 5 % mass loss, and interpreted as decomposition temperature.

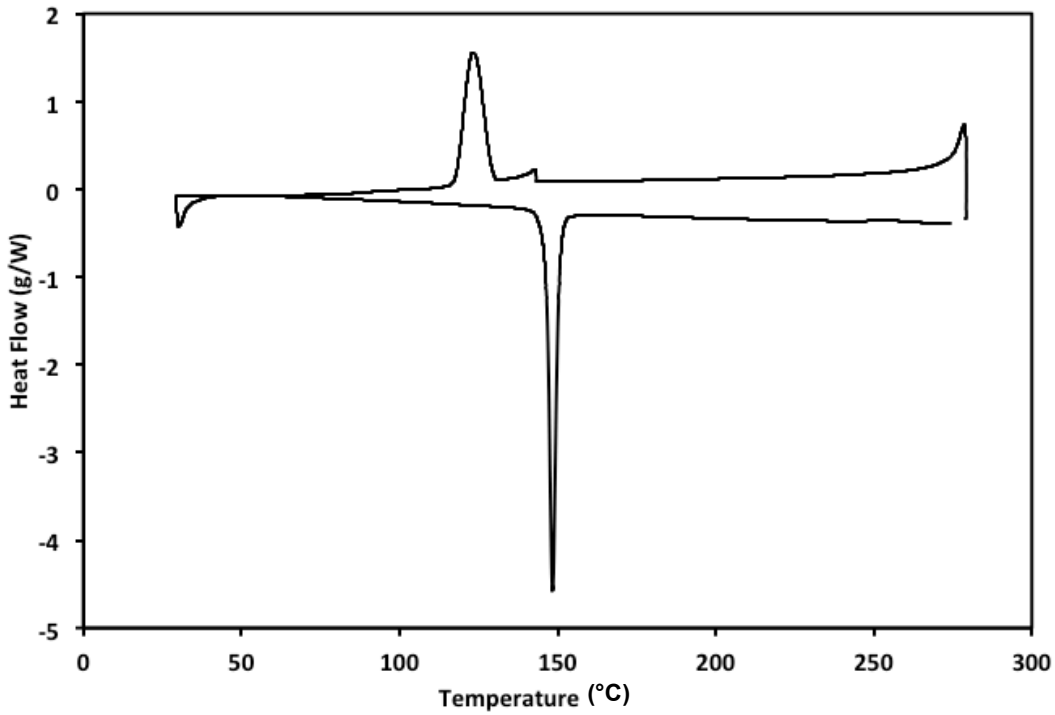

Figure 3-10. Differential scanning calorimetry plot for **3-1**.

Electronic properties: Molecular orbitals

	HOMO	LUMO
1-1a	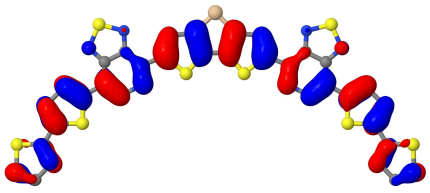	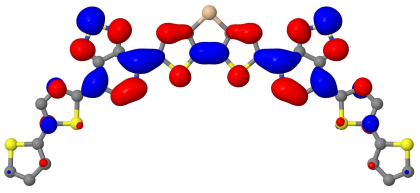

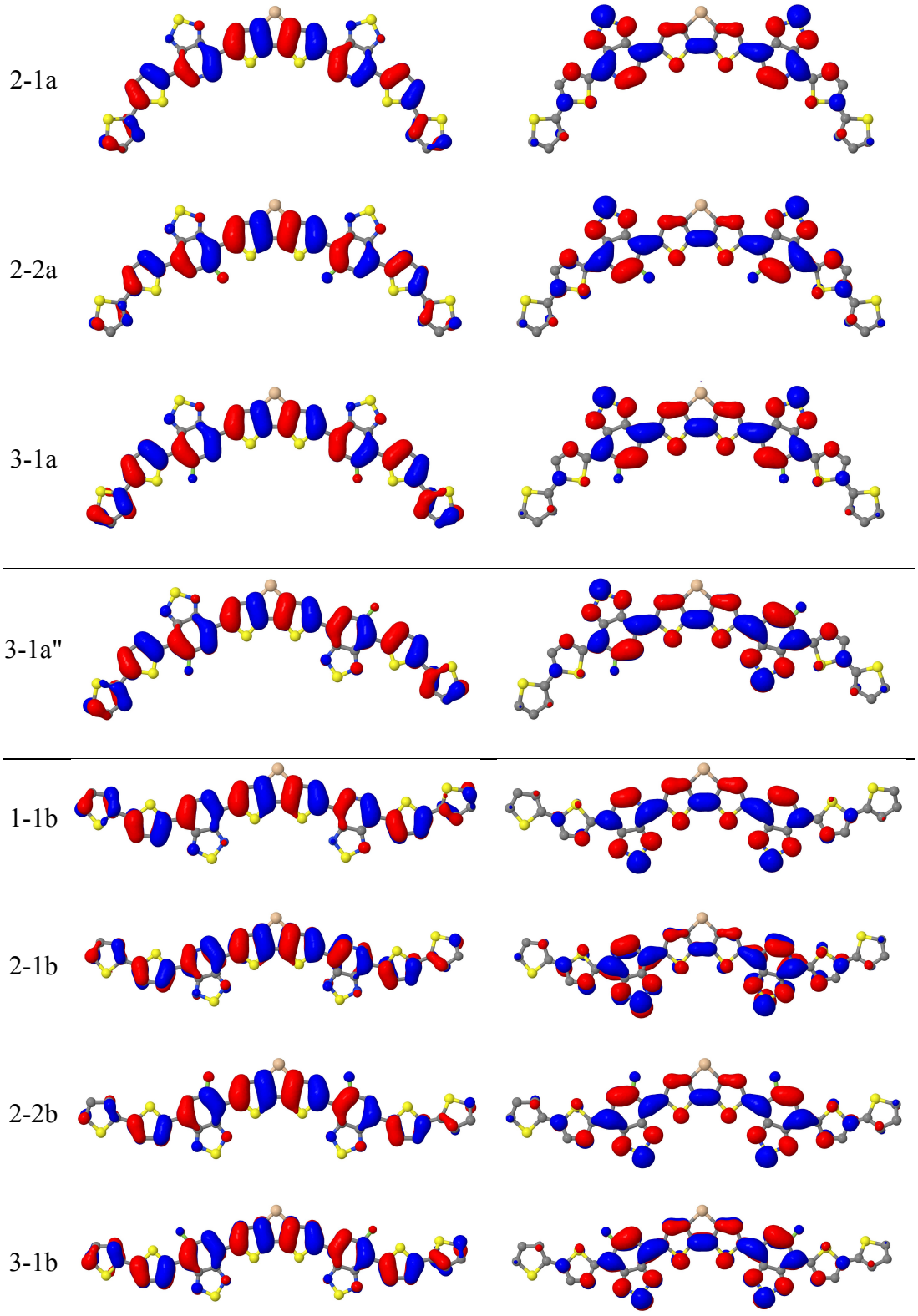
2-1a
2-2a
3-1a
3-1a"
1-1b
2-1b
2-2b
3-1b

Figure 3-11. HOMO and LUMO visualizations of the studied molecules (conjugated backbone in vacuum, CAM-3LYP/6-31g*). Hydrogens are not shown.

Electronic properties: Energies of different states

method	conjugated backbone						molecule					
	1-1a	2-1a	2-2a	2-2c	3-1a'	3-1b	1-1a	2-1a	2-2a	2-2c	3-1a'	3-1b
HOMO+IP (GS geom.)	0.15	0.14	0.13	0.13	0.18	0.17	0.09	0.08				
LUMO+EA (GS geom.)	-0.22	-0.23	-0.23	-0.23	-0.22	-0.22	-	-				
IP (relaxed geom.) [a]	5.44	5.31	5.22	5.19	5.38	5.31	5.30	5.14	5.09	5.09	5.27	5.18
IP (relaxed geom.) [a]							5.22	5.05	5.00	5.00	5.17	5.08
IP (experiment) [a]							**5.2**	**5.2**	**5.1**	**5.1**	**5.1**	**5.1**
EA (relaxed geom.) [a]	2.95	2.81	2.60	2.64	2.78	2.74	2.91	2.76	2.55	2.59	2.73	2.69
EA (relaxed geom.) [a]							3.04	2.88	2.67	2.77	2.80	2.81
EA (experiment) [a]							**3.6**	**3.6**	**3.3**	**3.3**	**3.4**	**3.4**
hole λ [a]	0.43	0.46	0.43	0.44	0.44	0.44	0.43	0.47	0.43	0.46	0.45	0.45
electron λ [a]	0.36	0.32	0.34	0.35	0.38	0.36	0.36	0.35	0.34	0.38	0.40	0.38
absorption (SS) [a]	2.32	2.34	2.46	2.42	2.45	2.40	2.26	2.31	2.40	2.40	2.42	2.37
absorption (LR) [a]	2.27	2.30	2.41	2.37	2.40	2.35	2.21	2.28	2.35	2.36	2.37	2.32
absorption (experiment) [a]							...	...	...	...	...	...
exciton λ (SS) [a]	0.51	0.53	0.53	0.55	0.54	0.54	0.50	0.58	0.53	0.58	0.55	0.54
exciton λ (LR) [a]	0.60	0.60	0.61	0.63	0.64	0.62	0.58	0.62	0.60	0.65	0.64	0.63
exciton λ (experiment) [a]							...	...	...	...	...	...
exciton binding energy [a]	0.53	0.52	0.55	0.51	0.55	0.55	0.49	0.44	0.51	0.49	0.52	0.51

For molecule 2-2b in dcm IP=4.99, EA=2.71.

Table 3-3. Energies (in eV) of different states (CAM-3LYP/6-31g*). In experiment conformations are not differentiated. Here λ means polaron reorganization energy (Stokes shift for exciton), GS = Ground State. [a]Calulation includes simulated chloroform environment. [b]Calulation includes simulated methylene chloride environment.

method	conjugated backbone						molecule					
	LC-ωPBE	ωB97X	6-31g	CAM-B3LYP	M062X	B3LYP	ωB97X	experiment	6-31g	CAM-B3LYP	M062X	B3LYP
HOMO+IP (GS geom.)	-	-0.47	0.05	0.15	0.35	0.84	-	0	0.06	0.09	0.30	0.78
LUMO+EA (GS	0.40	0.33	-0.14	-0.22	-0.39	-0.90	0.37	0	-	-	-0.36	-
IP[a] (relaxed geom.)			5.50	5.44			5.57		5.37	5.30	5.52	4.90
IP[b] (relaxed geom.)								**5.2**	5.29	5.22		
EA[a] (relaxed geom.)			3.44	2.95			2.78		3.39	2.91	3.05	3.16
EA[b] (relaxed geom.)								**3.6**	3.52	3.04		
hole[a] λ			0.52	0.43			0.50		0.52	0.43	0.45	0.20
electron[a] λ			0.38	0.36			0.58		0.38	0.36	0.31	0.14
absorption (SS)			2.04	2.32				...	1.98	2.26		
absorption[a] (LR)	2.89	2.69	2.00	2.27	2.28	1.52	2.64	...	1.93	2.21	2.23	1.46
exciton[a] λ (SS)			0.47	0.51				...	0.46	0.50		
exciton[a] λ (LR)	...	0.72	0.55	0.60	0.59	0.30		...	0.53	0.58		
exciton[a] binding energy			0.36	0.53					0.32	0.49		

For PBE functional HOMO+IP=1.11, LUMO+EA=-1.18.

Table 3-4. Energies (in eV) of different states for system 1-1a calculated by different methods. The basis set is 6-31g* except for "6-31g" column meaning CAM-B3LYP/6-31g. [a]Calulation includes simulated chloroform environment. [b]Calulation includes simulated methylene chloride environment.

Intra-molecular charge distribution

	X		Y		N-S-N group	
	NBO	ESP	NBO	ESP	NBO	ESP
1-1a	-0.46	-0.48	+0.27	+0.32	-0.31	-0.36
2-1a	+0.27	+0.30	-0.46	-0.47	-0.31	-0.36
2-2a	+0.12	+0.17	-0.01	-0.06	-0.35	-0.36
3-1a	-0.01	-0.09	+0.12	+0.18	-0.34	-0.36
1-1b	-0.45	-0.52	+0.27	+0.28/0.31	-0.31	-0.35
2-1b	+0.27	+0.25/0.31	-0.46	-0.45/0.48	-0.31	-0.39
2-2b	+0.12	+0.18	-0.01	-0.06	-0.34	-0.36
3-1b	-0.00	-0.16	+0.12	+0.23	-0.34	-0.35
3-1a"	-0.00	-0.12	+0.12	+0.24/0.15	-0.34	-0.34

Table 3-5. Atomic charges on X/Y groups and N-S-N groups belonging to the same closed π-shell molecular unit of a conjugated backbone in vacuum. NBO means charges obtained by Natural Bond Analysis, ESP means charges obtained by fitting electrostatic potential at the molecular van der Waals surface. For charge distribution with the asymmetry larger than 0.02 two numbers are given in correspondence with **Figure 3-11**.

Conformations: Relaxed energies

method	solv.	1-1a		2-2a	
		bb	mol.	bb	mol.
		planarized conjugated base			
B3LYP		2		2	
CAM-B3LYP		9		9	
ωB97X		17		17	
MP2		96		...	
MM3		130		251	
		dihedrals #3,4 are flipped			
ωB97X		119		38	
MP2		123		...	
CAM-B3LYP		129	128	46	32
B3LYP		132		34	
MM3		132		21	
ωB97X	clf	119		22	
CAM-B3LYP	clf	128	130	33	14
B3LYP	clf	128		19	
		dihedrals #1,3,4 are flipped			
ωB97X		147		65	
CAM-B3LYP		159	105	75	98
B3LYP		165		67	
ωB97X	clf	142	242	43	141
CAM-B3LYP	clf	155	102	59	77
B3LYP	clf	158	64	49	-47
		saddle point for dihedral #3			
ωB97X		377		169	
CAM-B3LYP		407		209	
B3LYP		468		253	

Table 3-6. Energies (in meV) of different conformations relative to the energy of the lowest energy conformation: dependence on method. The geometry is fully relaxed from crystalline geometry to local extremum. The default basis set is 6-31g*. Note that conformations with C_2 symmetry is slightly lower in energy than that with σ_h

symmetry (typically less than 1 meV difference). Here “bb” means conjugated backbone, “mol.” means the whole molecule. Entries are ordered by the third column (“1-1a bb”).

conformation		E(meV)	ΔE(meV)	d(D)	δ_1	δ_2	δ_3	δ_4	δ_5	δ_6
000000	(a)	0	-1	1.9	20	-11	0	0	11	-20
010000		12	0	2.3	21	163	-1	0	-11	20
010010		25	0	2.2	20	-163	1	1	-163	20
100000		28	-1	2.9	151	11	1	0	11	-19
110000		39	0	1.4	151	163	-1	0	-12	20
100010		40	-1	3.1	151	12	0	0	163	-19
110010		52	0	1.1	150	-163	1	1	-162	-21
100001		55	-1	3.4	151	11	1	1	11	151
001000		64	0	1.0	19	-11	179	-1	-13	20
110001		66	0	2.1	150	-163	1	0	-12	-151
010100		76	1	0.9	20	-164	0	180	-11	20
011000	(d)	78	0	1.0	21	163	179	0	11	-20
110011		78	1	0.4	150	-163	1	1	-163	150
011010		90	0	1.1	20	-164	-180	1	-163	20
101000		91	0	0.8	151	11	-179	1	13	-20
100100		92	0	2.2	152	14	1	-179	-10	20
110100		102	2	0.7	151	-162	1	-180	11	-20
101010		104	1	0.6	151	11	-180	1	-162	-21
111000		105	0	1.7	152	163	179	0	11	-20
100110		105	-1	2.4	151	12	0	180	163	-20
110110		117	1	0.8	150	-163	0	180	-164	20
111010		118	0	1.8	152	164	180	0	-163	-21
101001		119	0	1.3	152	10	179	-1	-14	-152
001100	(c)	128	1	0.7	20	-11	179	179	-11	20
110101		130	1	1.9	152	165	0	-180	-10	-151
111001		131	0	2.7	151	-163	-180	0	-12	-151
011100		143	-1	1.1	21	163	180	180	-11	20
111011		144	0	0.7	152	163	180	1	-163	151
101100	(b)	155	1	2.2	151	10	-180	-180	11	-20
011110		156	-1	0.8	20	-164	180	180	-164	20
111100		170	-1	0.7	151	-163	-180	-180	11	-20
101110		171	-1	2.4	151	11	-180	180	163	21
101101		182	2	3.4	151	10	-180	-180	10	151
111110		183	0	0.9	150	-163	-180	180	-164	20
111101		197	-1	1.5	151	163	180	180	11	151
111111		210	-1	1.0	152	164	180	180	164	152

Table 3-7. All the symmetry nonequivalent conformations of a conjugated backbone for molecule 1-1 in chloroform: energies, dipole moments, and dihedrals. Each

conformation is encoded by a sequence of 6 bits corresponding to the six dihedrals in Fig. 3-1; the bit is zero if the corresponding dihedral is closer to zero than to 180º. The third column gives the error of the independent rotation approximation. Conformations discussed in the details are highlighted.

conformation		E(meV)	ΔE(meV)	d(D)	δ_1	δ_2	δ_3	δ_4	δ_5	δ_6
000000	(a)	0	-1	2.1	17	0	-5	-5	0	17
001000		6	1	0.9	17	0	-162	7	0	17
001100	(c)	13	1	0.2	17	-1	160	160	-1	17
100000		28	-2	3.1	154	1	6	6	0	-17
101000		33	1	0.8	154	0	162	-7	0	-17
100100		34	0	2.0	154	0	-1	161	0	-17
101100	(b)	41	0	1.9	154	1	-161	162	0	-16
100001		57	-3	3.7	154	1	6	6	1	154
101001		62	0	0.9	154	1	-162	8	1	154
010000		64	-1	2.5	19	-180	-1	-8	0	17
101101		69	0	3.0	154	0	-161	-161	0	154
010100		70	1	1.4	19	180	-11	160	-1	16
011000	(d)	71	0	0.8	19	-180	-161	7	0	17
011100		78	0	1.0	19	-180	-162	-161	0	17
110000		91	0	1.1	153	-180	-5	0	0	-16
100010		92	-1	3.3	154	1	9	2	-180	-19
110100		96	2	0.5	153	-179	-2	162	0	-16
101010		98	1	0.2	154	1	-162	2	-180	-18
111000		98	0	1.7	153	-180	161	-6	0	-17
100110		100	-1	1.7	154	1	7	-161	-179	-18
111100		105	1	1.0	153	-180	-162	-161	1	-17
101110		106	-1	1.8	154	0	161	162	180	-20
110001		119	-1	2.2	153	-180	-4	-1	0	154
110101		124	2	1.4	153	-180	-2	162	0	154
111001		126	-1	2.2	153	180	161	-7	0	154
010010		127	0	2.7	19	179	5	5	179	19
111101		134	0	1.3	153	-179	-161	163	0	154
011010		136	-1	1.3	19	180	-163	3	179	19
011110		145	-2	0.9	19	-180	-161	-161	-180	19
110010		154	2	1.6	153	-179	-5	-6	-179	-19
110110		163	0	0.8	153	-180	-9	-163	-180	-18
111010		163	0	2.0	153	-180	-163	1	180	-19
111110		172	-2	0.8	153	-180	163	-162	-180	-18
110011		180	2	0.0	153	180	5	5	180	153
111011		189	1	1.0	153	-180	-163	1	180	153
111111		198	0	0.8	153	180	161	161	180	153

Table 3-8. All the symmetry nonequivalent conformations of a conjugated backbone for molecule 2-1 in chloroform.

conformation		E(meV)	ΔE(meV)	d(D)	δ_1	δ_2	δ_3	δ_4	δ_5	δ_6
000000	(a)	0	-1	1.3	20	-14	-1	-1	-14	20
010000		5	0	1.0	20	173	-1	0	-14	20
010010		11	1	0.4	21	173	-1	-1	173	21
001000		16	0	0.5	19	-12	-178	0	13	-20
010100		22	1	0.8	21	173	-2	176	11	-20
011000	(d)	23	-1	0.9	20	173	-178	0	14	-20
100000		27	-1	1.2	20	-15	0	-1	15	152
011010		28	0	0.2	20	-172	-178	1	172	-20
110000		32	0	2.3	19	-13	0	-1	-172	151
100010		32	0	1.2	20	172	-1	0	13	151
001100	(c)	33	0	0.6	20	-12	180	180	-12	20
110010		37	1	1.8	21	174	-1	1	-173	152
011100		40	0	0.4	21	173	179	178	12	-19
101000		43	0	1.9	20	-13	0	178	13	152
100100		43	0	1.0	20	-11	-180	0	-13	-151
011110		46	-1	0.1	20	173	-179	-179	173	20
101010		48	1	1.5	21	174	-2	175	11	152
110100		48	1	1.4	20	-11	-176	2	-173	152
100110		50	-1	1.2	20	173	-178	0	15	152
111000		50	-1	1.0	20	-14	0	179	173	152
100001		54	-1	0.7	152	14	0	0	14	152
111010		55	0	1.5	20	-170	1	-179	-171	152
110110		55	0	1.5	20	-172	-179	1	172	-151
110001		59	0	1.7	151	-172	-1	0	-13	-151
101100	(b)	59	1	0.9	19	-13	176	180	13	152
110011		65	0	3.0	152	173	-1	-1	173	152
101110		66	0	1.2	20	-172	-179	-176	12	151
111100		66	0	1.5	20	-11	-180	179	171	-152
101001		70	0	0.9	152	12	179	0	-13	-151
111110		73	-1	1.5	20	173	-178	178	-172	151
110101		75	1	2.8	152	-173	2	-175	-10	-152
111001		77	-1	1.4	152	171	179	-1	15	152
111011		82	0	1.2	152	171	178	-1	170	-152
101101		86	1	2.2	152	11	176	176	11	152
111101		93	0	0.6	152	171	178	177	-12	-151
111111		101	-1	2.2	152	-173	176	176	-173	152

Table 3-9. All the symmetry nonequivalent conformations of a conjugated backbone for molecule 2-2 in chloroform.

conformation		E(meV)	ΔE(meV)	d(D)	δ_1	δ_2	δ_3	δ_4	δ_5	δ_6
001000		0	1	2.0	20	0	168	-1	0	20
001100	(c)	1	0	2.1	20	0	-170	-170	0	20
000000	(a)	3	-2	1.4	19	0	-7	-7	0	19
010100		18	2	2.0	20	-179	-5	-173	0	20
011100		20	0	2.1	20	-180	169	169	0	20
010000		20	-1	1.8	20	-177	-5	0	0	20
011000	(d)	20	-1	1.7	19	-179	175	-5	0	19
101000		27	1	1.0	152	1	-168	1	0	-20
100100		27	1	2.7	152	0	-10	-169	0	-20
101100	(b)	27	1	1.3	152	-1	169	169	0	-20
100000		28	-1	2.6	152	1	13	14	1	-20
010010		37	1	1.8	20	-180	-2	-2	-180	20
011010		38	0	2.0	19	-178	174	-3	-178	21
011110		39	-1	1.9	19	-179	175	175	-179	19
101010		44	2	1.3	152	0	173	10	179	-20
110100		44	2	1.1	152	179	-5	173	-1	-20
111100		46	0	3.1	152	179	168	-169	0	-20
101110		46	0	0.7	152	1	-169	-168	-180	-20
110000		47	0	0.3	152	178	5	-1	0	-20
100010		47	-1	2.7	152	0	-1	6	177	-20
100110		47	-1	2.7	152	0	-3	-173	179	-19
111000		47	-1	3.0	152	-180	174	11	0	-19
101001		53	1	1.4	152	1	-169	-9	0	152
101101		54	0	0.4	152	0	178	178	0	152
100001		57	-3	3.2	152	0	1	1	0	152
110010		64	1	1.0	152	180	-8	8	179	-20
111010		64	0	3.1	152	179	169	8	178	-20
110110		64	0	0.5	152	178	3	-174	178	-19
111110		66	-1	3.1	152	-180	174	-173	179	-19
110101		71	2	0.9	152	180	-5	173	0	152
111101		73	0	1.8	152	178	168	-169	1	152
110001		73	0	1.7	152	-180	-5	1	0	152
111001		74	-1	3.5	152	180	-174	-11	-1	152
110011		90	1	0.8	152	179	-7	-7	179	152
111011		91	0	2.1	152	179	169	1	-180	152
111111		94	-2	3.9	152	-180	179	179	-180	152

Table 3-10. All the symmetry nonequivalent conformations of a conjugated backbone for molecule 3-1 in chloroform.

Conformations: Vibrations

CBB	diff.	ZPE	$E_{thermal}$
1	a-b	11	9
1	a-c	9	7
1	c-b	2	2
2	a-b	12	8
3	a-b	3	2
3	a-c	0.5	0.6
3	c-b	3	2
4	a-b	10	9

Table 3-11. Difference (in meV) in vibrational zero-point energy (ZPE) and thermodynamic energy at 300 K between two conformations indicated in the second column. Vibrational modes are calculated for planarized CBB, so that there are few imaginary frequencies. In all the "a-c" cases the mean square deviation between vibrational spectra is about 1 meV and the maximum deviation is 3-4 meV.

Conformations: PES scans

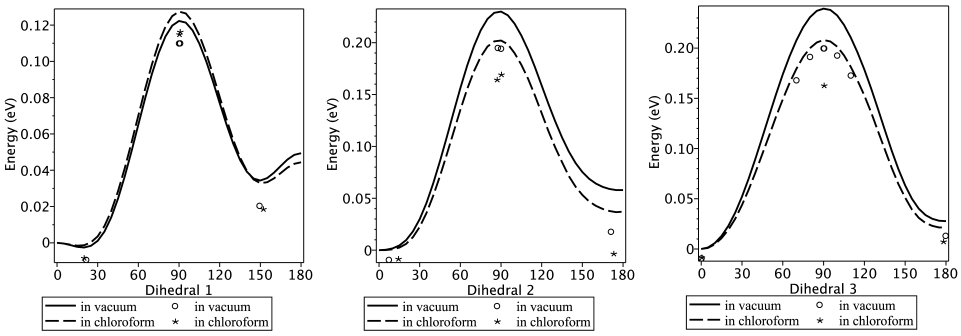

Figure 3-12. PES scans for dihedrals for the planarized conjugated backbone of molecule 2-2: dependence on solvent. Relaxed energies are shown as dots.

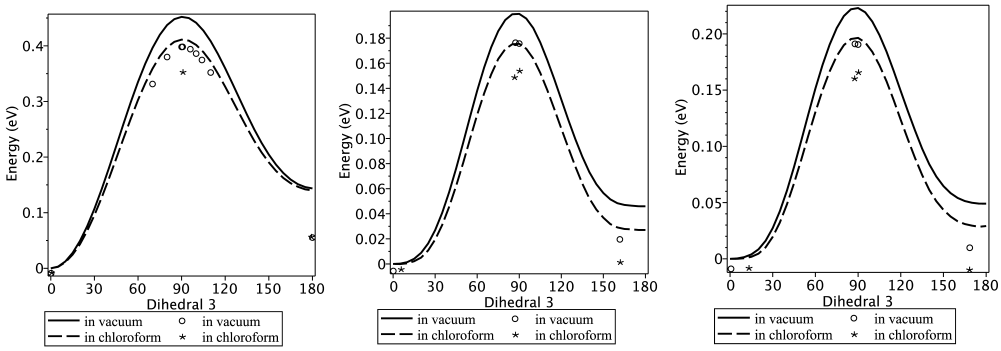

Figure 3-13. PES scans for dihedral 3 for molecules 1-1, 2-1, and 3-1.

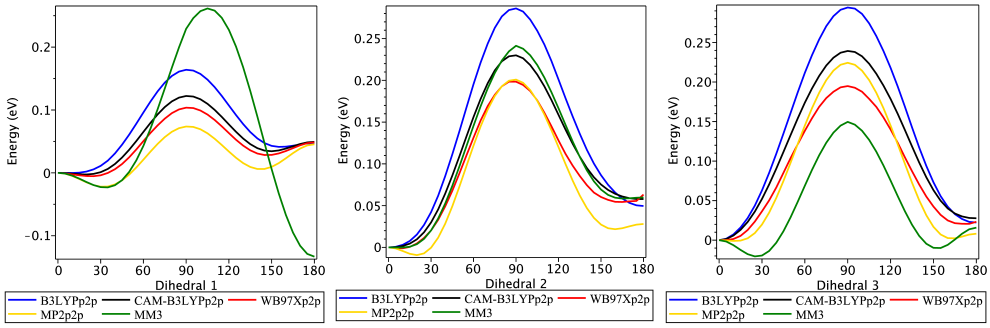

Figure 3-14. PES scans for dihedrals for the planarized conjugated backbone of molecule **2-2**: dependence on the method.

Conformations: MD sampling

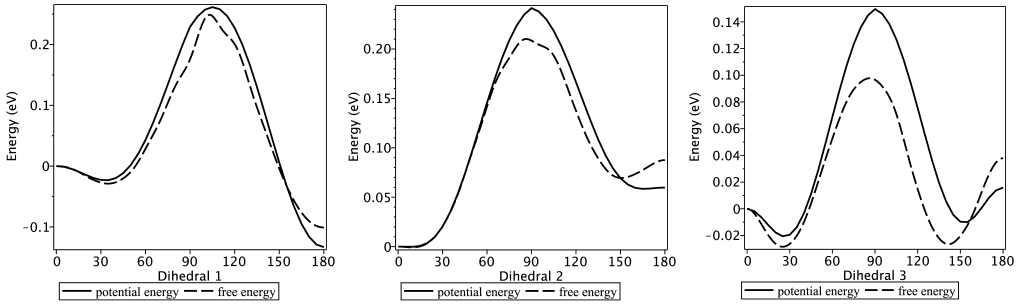

Figure 3-15. Free energy versus potential energy (unrelaxed) for dihedrals for molecule **2-2**.

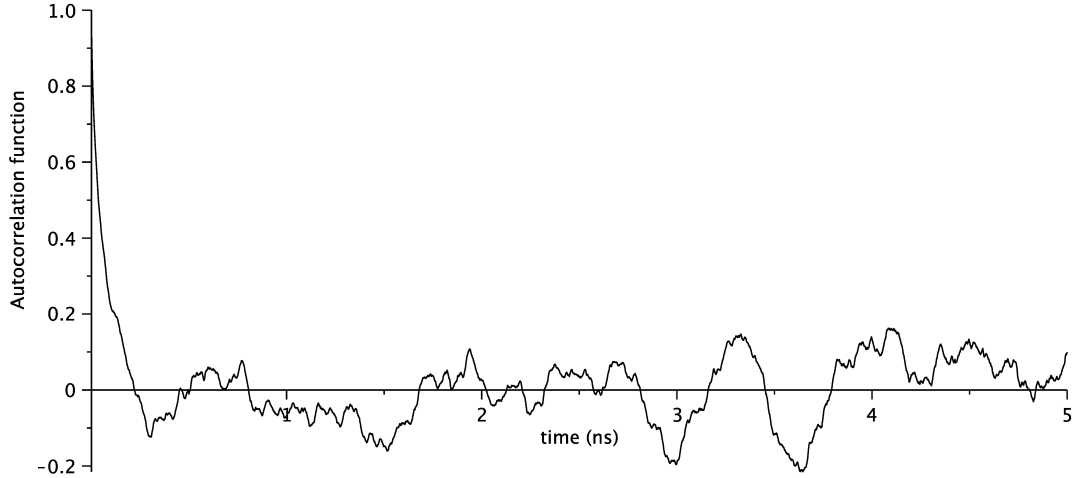

Figure 3-16. Autocorrelation function for dihedral 3 for molecule **2-2**.

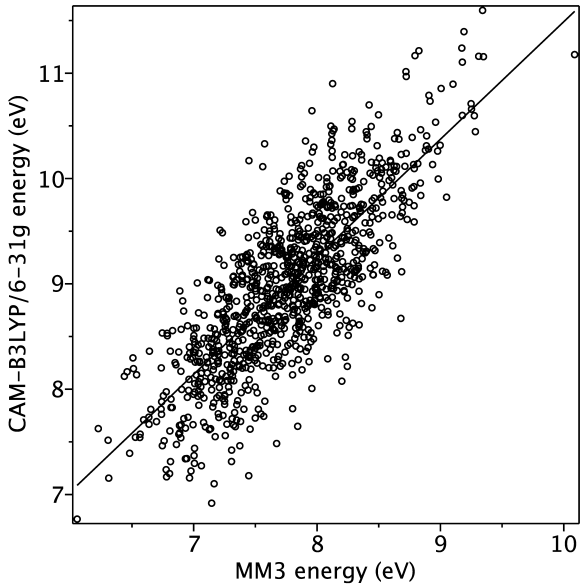

Figure 3-17. Correlation between MM3 and ab-initio energy for 1000 MD snapshots for molecule **2-2**.

Crystals

Table 3-12. Crystal data and structure refinement for molecule **2-2**.

Identification code	t1
Empirical formula	C64 H8 F2 N4 S8 Si
Formula weight	1155.31
Temperature	150(2) K
Wavelength	0.77490 Å
Crystal system	Triclinic
Space group	P-1
Unit cell dimensions	a = 9.2539(11) Å α = 81.005(9)°
	b = 14.9631(19) Å β = 85.178(9)°
	c = 22.219(3) Å γ =88.053(9)°
Volume	3027.3(6) Å3
Z	2
Density (calculated)	1.267 Mg/m3
Absorption coefficient	0.665 mm-1
F(000)	1160
Crystal size	0.15 x 0.03 x 0.00 mm3
Theta range for data collection	1.50 to 21.23°.
Index ranges	-8<=h<=8, -13<=k<=13, -20<=l<=20
Reflections collected	16271
Independent reflections	5158 [R(int) = 0.1010]
Completeness to theta = 21.23°	99.8 %
Max. and min. transmission	0.9980 and 0.9069
Refinement method	Full-matrix least-squares on F2
Data / restraints / parameters	5158 / 92 / 629
Goodness-of-fit on F2	1.347
Final R indices [I>2sigma(I)]	R1 = 0.1361, wR2 = 0.3409
R indices (all data)	R1 = 0.1795, wR2 = 0.3698
Largest diff. peak and hole	1.347 and -0.605 e.Å-3

Table 3-13. Crystal data and structure refinement for 3-1a.

Identification code	t2
Empirical formula	C64 H72 F2 N4 S8 Si
Formula weight	1219.82
Temperature	100(2) K
Wavelength	0.7749 Å
Crystal system	Triclinic
Space group	P -1
Unit cell dimensions	a = 8.808(3) Å α= 108.413(5)°
	b = 16.279(6) Å β= 100.019(6)°
	c = 22.976(9) Å γ = 95.249(5)°
Volume	3040.1(19) Å3
Z	2
Density (calculated)	1.333 Mg/m3
Absorption coefficient	0.456 mm-1
F(000)	1288
Crystal size	0.300 x 0.020 x 0.010 mm3
Theta range for data collection	2.920 to 25.094°.
Index ranges	-9<=h<=9, -17<=k<=17, -24<=l<=24
Reflections collected	20938
Independent reflections	8216 [R(int) = 0.0580]
Completeness to theta = 25.094°	98.3 %
Absorption correction	Semi-empirical from equivalents
Refinement method	Full-matrix least-squares on F2
Data / restraints / parameters	8216 / 524 / 875
Goodness-of-fit on F2	1.049
Final R indices [I>2sigma(I)]	R1 = 0.0661, wR2 = 0.1812
R indices (all data)	R1 = 0.0986, wR2 = 0.2010
Extinction coefficient	n/a
Largest diff. peak and hole	0.901 and -0.673 e.Å-3

Table 3-14. Crystal data and structure refinement for molecule 3-1b.

Identification code	rcb_t2_cs2_mek
Empirical formula	C40 H30 F0.25 N6 O2 S6 Si
Formula weight	851.90
Temperature	296(2) K
Wavelength	0.77490 Å
Crystal system	Triclinic
Space group	P -1
Unit cell dimensions	a = 9.2847(11) Å α = 80.301(9)°
	b = 14.9183(18) Å β = 78.544(8)°
	c = 22.514(3) Å γ = 87.708(8)°
Volume	3012.5(6) Å3
Z	4
Density (calculated)	1.878 Mg/m3
Absorption coefficient	0.554 mm-1
F(000)	1761
Theta range for data collection	1.51 to 23.88°.
Index ranges	-9<=h<=9, -15<=k<=15, -23<=l<=23
Reflections collected	22754
Independent reflections	6873 [R(int) = 0.1003]
Completeness to theta = 23.88°	95.3 %
Refinement method	Full-matrix least-squares on F2
Data / restraints / parameters	6873 / 96 / 624
Goodness-of-fit on F2	1.775
Final R indices [I>2sigma(I)]	R1 = 0.1890, wR2 = 0.4746
R indices (all data)	R1 = 0.2376, wR2 = 0.4918
Largest diff. peak and hole	0.959 and -0.799 e.Å-3

F. References (1) Gupta, V.; Kyaw, A. K.; Wang, D. H.; Chand, S.; Bazan, G. C.; Heeger, A. J. *Scientific reports* **2013**, *3*, 1965.

(2) Sun, Y.; Welch, G. C.; Leong, W. L.; Takacs, C. J.; Bazan, G. C.; Heeger, A. J. *Nat Mater* **2012**, *11*, 44.

(3) van der Poll, T. S.; Love, J. A.; Nguyen, T. Q.; Bazan, G. C. *Advanced materials* **2012**, *24*, 3646.

(4) Wang, N.; Chen, Z.; Wei, W.; Jiang, Z. *Journal of the American Chemical Society* **2013**, *135*, 17060.

(5) Welch, G. C.; Perez, L. A.; Hoven, C. V.; Zhang, Y.; Dang, X.-D.; Sharenko, A.; Toney, M. F.; Kramer, E. J.; Nguyen, T.-Q.; Bazan, G. C. *Journal of Materials Chemistry* **2011**, *21*, 12700.

(6) Dou, L.; You, J.; Hong, Z.; Xu, Z.; Li, G.; Street, R. A.; Yang, Y. *Advanced materials* **2013**, *25*, 6642.

(7) Cheng, Y.-J.; Yang, S.-H.; Hsu, C.-S. *Chem Rev* **2009**, *109*, 5868.

(8) Gendron, D.; Leclerc, M. *Energy & Environmental Science* **2011**, *4*, 1225.

(9) Lee, C. W.; Kim, O. Y.; Lee, J. Y. *Journal of Industrial and Engineering Chemistry*.

(10) Henson, Z. B.; Welch, G. C.; van der Poll, T.; Bazan, G. C. *Journal of the American Chemical Society* **2012**, *134*, 3766.

(11) Scharber, M. C.; Mühlbacher, D.; Koppe, M.; Denk, P.; Waldauf, C.; Heeger, A. J.; Brabec, C. J. *Advanced Materials* **2006**, *18*, 789.

(12) Vissenberg, M. C. J. M.; Matters, M. *Phys Rev B* **1998**, *57*, 12964.

(13) Horowitz, G. *J Mater Res* **2004**, *19*, 1946.

(14) Coropceanu, V.; Cornil, J.; da Silva, D. A.; Olivier, Y.; Silbey, R.; Bredas, J. L. *Chem Rev* **2007**, *107*, 926.

(15) Wang, L. J.; Nan, G. J.; Yang, X. D.; Peng, Q.; Li, Q. K.; Shuai, Z. G. *Chem Soc Rev* **2010**, *39*, 423.

(16) Kwon, S.; Wee, K.-R.; Kim, J. W.; Pac, C.; Kang, S. O. *The Journal of Chemical Physics* **2012**, *136*.

(17) Gring, M.; Gerlich, S.; Eibenberger, S.; Nimmrichter, S.; Berrada, T.; Arndt, M.; Ulbricht, H.; Hornberger, K.; Müri, M.; Mayor, M.; Böckmann, M.; Doltsinis, N. L. *Physical Review A* **2010**, *81*, 031604.

(18) Filatov, M. *Journal of Chemical Theory and Computation* **2013**, *9*, 4526.

(19) Balamurugan, D.; Aquino, A. J. A.; de Dios, F.; Flores, L.; Lischka, H.; Cheung, M. S. *The Journal of Physical Chemistry B* **2013**, *117*, 12065.

(20) Zhugayevych, A.; Postupna, O.; Bakus Ii, R. C.; Welch, G. C.; Bazan, G. C.; Tretiak, S. *The Journal of Physical Chemistry C* **2013**, *117*, 4920.

(21) Jackson, N. E.; Savoie, B. M.; Kohlstedt, K. L.; Olvera de la Cruz, M.; Schatz, G. C.; Chen, L. X.; Ratner, M. A. *Journal of the American Chemical Society* **2013**, *135*, 10475.

(22) Yum, S.; An, T. K.; Wang, X.; Lee, W.; Uddin, M. A.; Kim, Y. J.; Nguyen, T. L.; Xu, S.; Hwang, S.; Park, C. E.; Woo, H. Y. *Chemistry of Materials* **2014**.

(23) Jackson, N. E.; Savoie, B. M.; Kohlstedt, K. L.; Marks, T. J.; Chen, L. X.; Ratner, M. A. *Macromolecules* **2014**, *47*, 987.

(24) Lee, W.; Kim, G.-H.; Ko, S.-J.; Yum, S.; Hwang, S.; Cho, S.; Shin, Y.-H.; Kim, J. Y.; Woo, H. Y. *Macromolecules* **2014**, *47*, 1604.

(25) Lee, J. B.; Kim, K. H.; Hong, C. S.; Choi, D. H. *Journal of Polymer Science Part A: Polymer Chemistry* **2012**, *50*, 2809.

(26) Zheng, N.; Li, H.; Sun, G.; Zhong, K.; Yin, B. *Organic & Biomolecular Chemistry* **2013**, *11*, 5100.

(27) Zhou, J.; Wan, X.; Liu, Y.; Long, G.; Wang, F.; Li, Z.; Zuo, Y.; Li, C.; Chen, Y. *Chemistry of Materials* **2011**, *23*, 4666.

(28) Diallo, A. K.; Metri, N.; Brunel, F.; Sallenave, X.; Goubard, F.; Margeat, O.; Ackermann, J.; Videlot-Ackermann, C. *Synthetic Metals* **2013**, *184*, 35.

(29) Sugita, Y.; Okamoto, Y. *Chemical Physics Letters* **1999**, *314*, 141.

(30) Yanai, T.; Tew, D. P.; Handy, N. C. *Chemical Physics Letters* **2004**, *393*, 51.

(31) Baer, R.; Livshits, E.; Salzner, U. *Annual Review of Physical Chemistry* **2010**, *61*, 85.

(32) Cossi, M.; Rega, N.; Scalmani, G.; Barone, V. *Journal of Computational Chemistry* **2003**, *24*, 669.

(33) Frisch, M. J.; etal *Gaussian 09, revision A.1*; Gaussian, Inc.: Wallingford CT, 2009.

(34) Allinger, N. L.; Li, F.; Yan, L.; Tai, J. C. *Journal of Computational Chemistry* **1990**, *11*, 868.

(35) Ponder, J. W. *TINKER 6.2,* http://dasher.wustl.edu/tinker.

(36) Coffin, R. C.; Peet, J.; Rogers, J.; Bazan, G. C. *Nat Chem* **2009**, *1*, 657.